Review Article

Aiping Gao*, Si-Han Zhao, Jiajia Wang and Hai-Lou Li*

State-of-the-art of polyoxometalate-based catalysts for catalytic removal of vesicants

https://doi.org/10.1515/revic-2025-0047
Received May 19, 2025; accepted July 21, 2025;

Abstract: Vesicants are one frequently-used kind of chemical warfare agents due to their low-boiling point, high gaseous diffusion, and accessibility. Sulfur mustard is one of the main vesicant that has since been banned by international organization, but there are still large stocks in some countries and its production is relatively easy, requiring no tedious steps or expensive equipment. Thus far, catalytic oxidation, alongside physical adsorption and hydrolysis has been proven one of the most effective methods for decontaminating the HD simulant, 2-chloroethyl ethyl sulfide (CEES). POMs have exhibited outstanding catalytic oxidation performance toward CEES owing to their unique redox properties, robust structural stability, flexible metal valence and the presence of numerous active sites. This review summarizes the advances of POM-based materials for catalytic decontamination of vesicants simulant CEES, including POMs, POM-based MOFs and POMs composites. This review provides new sights for engineering robust POM-based catalysts for the catalytic decontamination of CWAs.

Keywords: polyoxometalate; POM-based catalysts; catalytic decontamination; vesicants

1 Introduction

Chemical warfare agents (CWAs) still can bring a potential threat to mankind owing to their abuse in wars and terrorist attacks.[1–3] Vesicants as a main category of CWAs, such as sulfur mustard (HD), are commonly used CWAs owing to their ready and cheap procurement, these can cause serious skin blisters, irritation to the respiration system and eyes, DNA damage through alkylation, and even death.[4–6] Therefore, it is essential to develop novel and efficient materials for the decontamination of vesicants. According to molecular structure characteristics of vesicants, the primary decomposition strategy is oxidation.[7] A series of different materials including metal-organic frameworks (MOFs),[8] metal-coordinated porous organic polymer,[9] metal NHC complexes,[10] covalent organic frameworks,[11] covalent-triazine frameworks,[12] TiO_2-based materials,[13] zeolites,[14] and metal oxides,[15,16] and polyoxometalates (POMs)[17] have been designed for the removal of vesicants based on adsorption or catalytic decontamination. Comparing with adsorption removal mode, catalytic decontamination has been prevailed due to its outstanding feature of high efficiency, celerity, and repeatability. For vesicants such as HD, selective oxidization into non-toxic sulfoxide products is the primary means. Furthermore, exposure incidents to CWAs can occur via the gas, aerosol, liquid, or gel-like “thickened” composites of the agent.

POM chemistry has developed for almost 200 years after Berzelius reported the first POM $[PMo_{12}O_{40}]^{3-}$ in 1826 .[18] The desirable physical and chemical properties of POMs such as size, structure, photochemistry, redox ability, and charge distribution can be regulated through the introduction of different heteroatoms, organic components and varying structural dimensions from one-to three-dimensional forms.[19–22] POMs based on Mo, W, Nb, V, Ta, Al, and other elements have been widely prepared.[23–26] POMs are broadly used in many fields such as proton conductive materials,[27] removal of environmental pollutants,[28] biology as anticancer[29] and catalysis,[30,31] supramolecular materials,[32] colloid science,[33] energy,[34] electro/photochromic systems,[35,36] sensors,[37] and magnetism[38] through interdisciplinary. Due to their tunable acid-base and reversible multi-electron redox properties of POMs, POMs and the post-modified POMs-based composite exhibit notable catalytic performance in a wide range of reactions including

---

***Corresponding authors: Aiping Gao and Hai-Lou Li**, College of Chemistry and Chemical Engineering & Henan Province Key Laboratory of Utilization of Non-Metallic Mineral in the South of Henan, Green Catalysis and Synthesis Key Laboratory of Xinyang, Xinyang Normal University, Xinyang, Henan, 464000, P.R. China, E-mail: gaoapchem@163.com (A. Gao), lhl@xynu.edu.cn (H.-L. Li). https://orcid.org/0000-0002-5723-7557 (A. Gao)
Si-Han Zhao and Jiajia Wang, College of Chemistry and Chemical Engineering & Henan Province Key Laboratory of Utilization of Non-Metallic Mineral in the South of Henan, Green Catalysis and Synthesis Key Laboratory of Xinyang, Xinyang Normal University, Xinyang, Henan, 464000, P.R. China

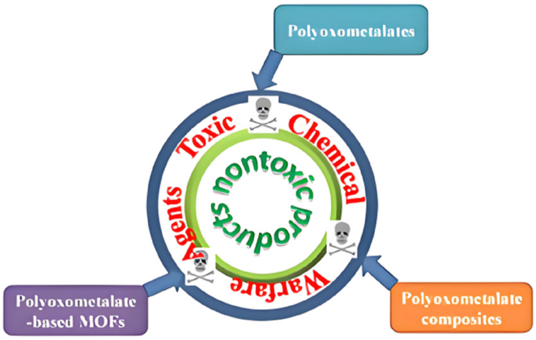

Figure 1: POM-based materials for catalytic decontamination of vesicants.

esterification, hydrolysis, and oxidation of organic compounds.[39,40] Different kinds of POM-based materials have been designed and prepared for the catalytic decontamination of vesicants, but that still have some challenges even though great progress has been made (Figure 1). It is of great necessity to review the advances in the catalytic decontamination of vesicants by POM-based catalysts for aiming to propel further progress.

2 POM-based compounds for catalytic decontamination of vesicants

Vesicants were frequently-used CWAs due to their low-boiling point, high gaseous diffusion, and accessibility.[41] Although not as lethal as other CWAs, their use causes prolonged pain that would often be followed by death. The heavy use of vesicants led to extreme suffering in the Second World War.[42] Sulfur mustard is one of the main vesicant that has since been banned by international organization, but there were still large stocks in some countries and its production is relatively easy, requiring no tedious steps or expensive equipment. Thus far, catalytic oxidation, alongside physical adsorption and hydrolysis has been proven on of the most effective methods for decontaminating the HD simulant, 2-chloroethyl ethyl sulfide (CEES). POMs have exhibited outstanding catalytic oxidation performance toward CEES owing to their unique redox properties, robust structural stability, flexible metal valence and the presence of numerous active sites. This section summarizes the advances of POM-based materials for catalytic decontamination of vesicants simulant CEES, including POMs, POM-based MOFs and POMs composites.

2.1 POMs in firsthand catalytic decontamination of vesicants

An's group designed four carboxylic acid modified POMs in the form of $Cs_4\,[M(H_2O)_4][PMo_6O_{21}(PABA)_3]_2{\cdot}nH_2O$ (M = Co, Mn, Ni, Zn, PABA = *p*-aminobenzoic acid) (**$CoPMo_6O_{21}$**, **$MnPMo_6O_{21}$**, **$NiPMo_6O_{21}$**, **$ZnPMo_6O_{21}$**) for selective catalytic oxidation of thioethers including CEES (Figure 2).[43] These four hybrid POMs displayed similar dimeric isostructural architectures. The synthesis of corresponding POMs using K^+, Cs^+, and Rb^+ were attempted, but only Cs worked. Further, different metal cations and organic ligands were used to synthesize different POMs, and only Co^{2+}, Mn^{2+}, Ni^{2+}, and Zn^{2+} and PABA were suitable. Four POMs were crystallized in space group P1 constructed from polyoxoanion units $\{PMo_6O_{21}\}$. Using methyl phenyl sulfide model, **$CoPMo_6O_{21}$** could efficiently catalyse its oxidation into the corresponding sulfoxide with the selectivity of 98 % in 20 min, which displayed the highest activity of the catalysts. Minimal methyl phenyl sulfide was converted by both PABA and $CoCl_2$, and $Cs_3\,[PMo_6O_{21}(PABA)_3]{\cdot}nH_2O$ could catalyse 72 % of methyl phenyl sulfide with a selectivity of 89 %, far inferior to **$CoPMo_6O_{21}$**. This result showed the synergistic effect of Co site and PABA-modified POMs together was responsible for the rapid reaction rate and excellent selectivity. Similar results were found using $\{CoAsMo_6(PABA)_3\}$ and $\{CoTeMo_6(PABA)_3\}$, indicating that the central heteroatoms affected the selectivity (in the order of PMo > AsMo > TeMo). Red shifts and a new band at 760 nm in the UV–vis absorption spectrum of the interaction between **$CoPMo_6O_{21}$** and H_2O_2 indicated the generation of active peroxomolybdenum and peroxocobalt species, which attacked the S atom of the sulfides to yield the corresponding product. The conversion of various organic sulfides did not obviously decrease with the electronic and steric-hindrance changes. The oxidation reaction by **$CoPMo_6O_{21}$**, **$MnPMo_6O_{21}$**, **$NiPMo_6O_{21}$**, and **$ZnPMo_6O_{21}$** were first-order reactions with corresponding kinetics constants of 0.23842, 0.1624, 0.20015, and 0.17483 min^{-1}, respectively. When methyl phenyl sulfide was replaced with the mustard gas simulant, CEES, 98.8 % was oxidized by **$CoPMo_6O_{21}$** into the nontoxic CEESO with 99.0 % selectivity in 12 min. The recyclability and stability of this system was also well demonstrated during the selective oxidation of CEES.

Zhou's group employed four nanopolyoxometalate clusters $Na_8K_{14}(VO)_2\,[K_{10}\subset\{Mo(Mo)_5O_{21}(H_2O)_3(SO_4)\}_{12}\{(VO)_{30}(H_2O)_{20}]$ (denoted **$\{Mo_{72}V_{30}\}$**),[44] ($[\{Na_{10}(H_2O)_{12}\subset\{Mo_{72}Cr_{30}O_{252}(CH_3COO)_{19}(H_2O)_{94}\}]{\cdot}ca.120{\cdot}H_2O$ (denoted **$\{Mo_{72}Cr_{30}\}$**),[45] $[Mo_{72}Fe_{30}O_{252}(CH_3COO)_{10}\{Mo_2O_7(H_2O)\}\{H_2Mo_2O_8(H_2O)\}_3(H_2O)_{91}]{\cdot}ca.140{\cdot}H_2O$ (denoted **$\{Mo_{72}Fe_{30}\}$**),[46]

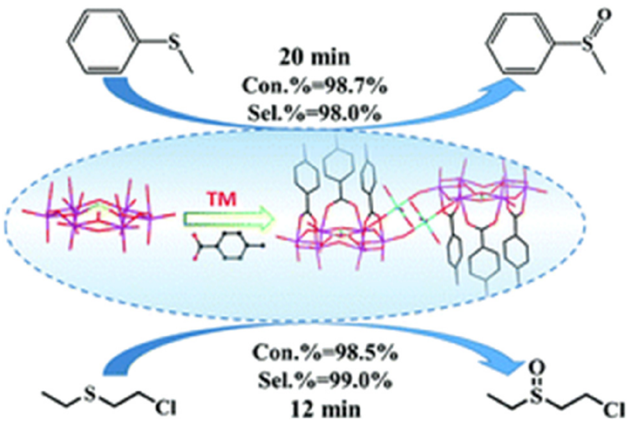

Figure 2: The schematic diagram of catalytic oxidation of thioethers including CEES by $MPMo_6O_{21}$ (M = co, Mn, Ni, Zn). Reproduced with permission from ref. 43. Copyright 2020 The royal society of Chemistry.

$[\{Mo(Mo)_5O_{21}(H_2O)_4CH_3COO\}_{12}\{MoO(H_2O)\}_{30}]\cdot$ca. $150\cdot H_2O$ (denoted **{Mo_{102}}**)[47] to catalyse the decontamination of HD and CEES.[48] The conversion rate of CEES (0.042 mmol, 5 μL) reached 99.45 % in 10 min using 10.0 mg (0.53 μmol) of **{$Mo_{72}Cr_{30}$}** at approximately 20 °C. The optimal molar ratio of H_2O_2: CEES was determined to be 1:1. Within the reaction time of 1.0 min, the conversion of CEES was 51.42 %, 45.65 %, 38.38 %, and 34.95 % for **{$Mo_{72}V_{30}$}**, **{$Mo_{72}Cr_{30}$}**, **{$Mo_{72}Fe_{30}$}**, and **{Mo_{102}}**, respectively. A good linear relationship between $\ln(C_t/C_0)$ (C_0 and C_t was the concentrations of CEES at the start and time t) and the reaction time indicated first-order reaction kinetics with the kinetic constants of **{$Mo_{72}V_{30}$}**, **{$Mo_{72}Cr_{30}$}**, **{$Mo_{72}Fe_{30}$}**, and **{Mo_{102}}** of 0.56, 0.53, 0.47, and 0.44 min^{-1}, respectively and the following catalytic activity order: V > Cr > Fe > Mo. The reversible oxidation peak potentials with the addition of H_2O_2 and the further addition of the substrate CEES demonstrated that the intermediates generated from nodal metal interaction with H_2O_2 implemented the selective oxidation of CEES to CEESO. The unchanged Mo^{VI}3d X-ray photoelectron spectroscopy (XPS) peaks of **{$Mo_{72}V_{30}$}** indicated that Mo^{VI} did not participate in the catalytic reaction. Conversely, the binding energies of V 2p at 516.48 and 523.96 eV assigned to V^{IV} $2p_{3/2}$ and V^{IV} $2p_{1/2}$ were shifted to 516.40 eV (V^{IV} $2p_{3/2}$), 517.49 eV (V^{V} $2p_{3/2}$), 523.37 eV (V^{IV} $2p_{1/2}$), and 524.71 eV (V^{V} $2p_{1/2}$) with H_2O_2 addition, which showed that V was oxidized to a higher valence state by H_2O_2.[49] With the simultaneous addition of H_2O_2 and CEES to the solution of **{$Mo_{72}V_{30}$}**, XPS peaks of V 2p were recovered, demonstrating that the catalyst recovered its original state. A similar situation was observed with the three other catalysts. The desired fast degradation of CEES by four catalysts benefitted from the large oil–water interface area due to agitation and the full exposure of active sites in **{$Mo_{72}M_{30}$}**. All four catalysts exhibited outstanding reusability, and the conversion rates of CEES still reached 93.41 %, 90.50 %, 90.13 %, and 89.70 % for **{$Mo_{72}V_{30}$}**, **{$Mo_{72}Cr_{30}$}**, **{$Mo_{72}Fe_{30}$}**, and **{Mo_{102}}**, respectively after five cycles.

Zhou's group prepared an organic functional POM $[C_{44}H_{28}N_4Cl_4]_{1\cdot5}$ $[H_2PMo_{10}V_2O_{40}]\cdot 2C_2H_6O$ (**H_2TClPP-H_2PVMo**) by ion-exchange between 5,10,15,20-tetra(4-chlorine)phenylporphyrin (TClPP) and $H_5PV_2Mo_{10}O_{40}$ (**H_5PVMo**) for photocatalytic degradation of CEES .[50] A higher singlet oxygen generation capacity was observed for **H_2TClPP-H_2PVMo** than for TClPP, which laid solid foundation for the selective oxidization of CEES to nontoxic CEESO. The red-shift of characteristic bands of P-Oa and the blue-shift of characteristic bands of Mo-Ob-Mo and Mo-Oc-Mo in the Fourier-transform infrared (FTIR) spectrum of **H_2TClPP-H_2PVMo** indicated the formation of hybrid **H_2TClPP-H_2PVMo**, which was further verified by the ^{31}P solid-state nuclear magnetic resonance (NMR) spectrum. Spectrometric titration results of H_5PVMo solution by TClPP showed a nonequality to the simple sum of the UV spectrum of TClPP and **H_5PVMo**, which indicated that both had strong interactions and TClPP was converted to a deprotonated salt. An obvious turning point indicated that a stable hybrid was formed between TClPP and **H_5PVMo** at the stoichiometric ratio of 1:1.5; elemental analysis and thermogravimetric analysis (TGA) results confirmed this result. Within 180 min, the degradation rate of CEES by **H_2TClPP-H_2PVMo** in methanol could reach 99.52 % with irradiation and 28.24 % without irradiation, showing that light significantly accelerated the decontamination of CEES by **H_2TClPP-H_2PVMo**. At the same catalytic conditions, the degradation rates of CEES were approximately 20 % and 55.31 % for **H_5PVMo** and TClPP, respectively. In view of the hydrolysis effect on HD and CEES, the degradation of CEES by **H_2TClPP-H_2PVMo** in methanol/water (1:1, v/v) was also explored. The degradation rate of CEES by **H_2TClPP-H_2PVMo** reached 99.14 % with irradiation and 91.05 % within 90 min (under irradiation). The degradation rate of 98.1 % in methanol/water (1:1, v/v) was still achieved after the fifth *in situ* circulation, indicating the good repeatability of **H_2TClPP-H_2PVMo**. Under irradiation but no catalyst in air, CEES could be alcoholised to 2-methoxyethyl ethyl sulfide in methanol, and hydrolysed to ethyl 2-hydroxyethyl sulfide (HEES) because of a small amount of water in methanol. Active oxygen generated from **H_2TClPP-H_2PVMo** selectively oxidized CEES and HEES to CEESO and ethyl hydroxyethyl sulfoxide (HEESO) under irradiation. In addition, 2-methoxyethane and ethyl sulfide were possibly produced in methanol/water (1:1, v/v) via the alcoholysis and hydrolysis of CEES.[51,52] Active oxygen trapping experiments using benzoquinone (BQ) or NaN_3, revealed that CEES was degraded by $O_2^{\cdot-}$and $^1O_2$ producing from **H_2TClPP-H_2PVMo** in methanol with visible light irradiation. The $^1O_2$ quantum yield of TClPP was significantly increased from 0.35 to 0.73 of **H_2TClPP-H_2PVMo** in methanol. The fluorescence intensity of **H_2TClPP-H_2PVMo** was greatly reduced because it dissipated more energy to complete energy transfer from the singlet state to the excited triplet state under irradiation.[53] This material could degrade CEES under visible light irradiation.

Yang's group successfully prepared a novel 12-Ti-substituted POM $K_{10}H_{15}$ [{$K_2Na(H_2O)_3$}@{$(Ti_2–O)_2(Ti_4O_4)_2$ (*A*-*α*-1,3,5-GeW_9O_{36})$_2$ (*A*-*α*-2,3,4-GeW_9O_{36})$_2$}]·45H2O (**TiGeWO**) with the key characteristic of chiral trivacant Keggin-type GeW_9O_{36} (***A*-*α*-1,3,5-GeW_9O_{36}** and ***A*-*α*-2,3,4-GeW_9O_{36}**) units.[54] Two ***A*-*α*-1,3,5-GeW_9O_{36}** and two ***A*-*α*-2,3,4-GeW_9O_{36}** were connected via two Ti_2O and two Ti_4O_4 alternate bridging cluster cores, which was the first time for the coexistence of Ti_2O and Ti_4O_4 cores as the bridges in POM. Each Ti atom in the Ti_4O_4 tetrad was coordinated with three μ_2-O, one μ_4-O in the GeW_9O_{36} unit, and two μ_2-O in the Ti_4O_4 core. The two Ti atoms of the Ti_2O core were coordinated by four μ_2-O, one μ_4-O in the GeW_9O_{36} unit, and one μ_2-O in the Ti_2O core. Although the trivacant ***A*-*α*-1,3,5-GeW_9O_{36}** and ***A*-*α*-2,3,4-GeW_9O_{36}** segments were chiral enantiomers, they coexisted in **TiGeWO**, resulting in a non-chiral overall structure. **TiGeWO** has been applied in the heterogeneous catalytic oxidation of various aromatic thioethers with H_2O_2 as an oxidant in acetonitrile at 60 °C. **TiGeWO** could efficiently catalyze the oxidation of various substrates into sulfoxides or sulfones. Substrates with electron-donating groups on the aromatic ring exhibited a higher conversion rates than those with electron-withdrawing groups. Additionally, larger steric hindrance could reduce the conversion and selectivity. The catalytic decontamination of CEES by **TiGeWO** was investigated under H_2O_2 as oxidizer at 30 °C. Nearly 100 % of CEES could be oxidized to CEESO in 90 min. The linear relation between ln (C_t/C_0) suggested that this was a first-order reaction with a kinetic constant k_1 of 0.05197 min^{-1} and a half-life of approximately 13 min. After three cycles, the high catalytic conversion of aromatic thioethers and CEES was retained, and the unanimous IR spectra of **TiGeWO** after three cycles demonstrated its good reusability.

Overcoming the inactivity of oxoboron clusters and the repulsion between negative polyoxotungstates and oxoboron clusters has been a challenge in the creation of B-containing polyoxotungstates. recently, Zheng and Yang's group developed B_{30}-incorporated polyoxotungstates $[(B_{18}Si_3Ln_6O_{36}(OH)_{14})\{B_4Ni_4O_{10}(OH)(A\text{-}\alpha\text{-}SiWO_{34})\}_3]^{44-}$ (**1Ln**) $[(B_{19}Si_2Ln_7O_{35}(O–H)_{15}(H_2O))\{B_4Ni_4O_{10}(OH)_4\ (A\text{-}\alpha\text{-}SiW_9O_{34})\}_2\{B_3Ni_4O_9\ (OH)_3\ (A\text{-}\alpha\text{-}SiW_9O_{34})\}]^{41-}$ (**2Ln**, Ln = Gd, Tb and Dy), and B_{22}-incorporated POTs $[(B_{22}O_{42})\{LnNi_3(OH)_3(B\text{-}\alpha\text{-}SiW_9O_{34})\}_4]^{34-}$ (**3Ln**; Ln = Sm, Gd and Tb) through multicomponent charge and symmetry matching among Ln^{3+}, TM^{2+}, borates, and polyoxotungstates.[55] To date, **1Ln** and **2Ln** were the largest B-containing polyoxotungstates. B-rich polyoxotungstates **1Ln**, **2Ln** and **3Ln** were prepared using $NaBO_3·4H_2O$, $Li_2B_4O_7$ and $K_2B_{10}O_{16}·8H_2O$ as the sources of B, respectively. **1Gd**, **2Gd**, and **3Gd** were discussed in detail as representatives (Figure 3). In **1Gd**, 30 B atoms were dispersed over two $B_9O_{15}(OH)_6$ ({B_9}) nonamers, three $B_2O_4(OH)_2$ ({B_2}) dimers, and six BO_3 monomers with a new B–O nonamer appearing in {B_9}. A unique trigonal-prism cage $[B_{18}Si_3O_{36}(OH)_{12}]^{18-}$ ({$B_{18}Si_3$}) was formed by two {B_9} assemblies in a foot-to-foot orientation and three SiO_4 tetrahedra connected by six B–O–Si bridges. The anionic, hollow {$B_{18}Si_3$} cage was encapsulated by two cationic planar triangular $[Gd_3\ (\mu_3\text{-OH})]^{8+}$ units in its inner cavities through coordination with O from the {$B_{18}Si_3$} cage, and forming the $[B_{18}Si_3Gd_6O_{36}(OH)_{14}]^{2-}$ ({$B_{18}Si_3Gd_6$}) cluster. In this cluster, the innermost Gd-shell $Gd_6O_{12}(OH)_2$ ({Gd_6}) with trigonal prismatic shape was formed. Six BO_3 units in **1Gd** served as bridges, bonding to both Ni^{2+} and Gd^{3+} ions. For the 12 Ni^{2+} ions in the Ni-shell, every four Ni^{2+} ions were arranged in a pyramidal array, and two μ_3-OH groups, two BO_3 units, and one {B_2} dimer are bridged by adjacent Ni^{2+} ions to form $B_4Ni_4O_{10}(OH)_4$ ({B_4Ni_4}). Three Ni-substituted polyoxotungstate motifs $[B_4Ni_4O_{10}(OH)_4](A\text{-}\alpha\text{-}SiW_9O_{34})$ ({B_4Ni_4(A-SiW_9)}) were formed after the introduction of {B_4Ni_4} clusters in the vacant sites of [A-SiW_9]. The B30-incorporated **1Gd** was obtained with the {$B_{18}Si_3Gd_6$} cluster surrounded by three {B_4Ni_4(A-SiW_9)} motifs. Owing to the multicomponent cooperative charge-matching interactions and matched geometries between components, a multi-shell configuration of Ln-shell@B-shell@Ni-shell@W-shell ({Gd_6}@{$B_{24}Si_3$}@{Ni_4}$_3$@{SiW_9}$_3$) was existed in **1Ln** polyoxotungstates series. The robust coordination ability and flexible coordination modes of Gd^{3+} ions used as templates possessed fewer structural restrictions on the formation of oxoboron motifs and their architectures. The long Gd–O bond, high coordination number and positive charge of Gd^{3+} ion were crucial for constructing larger B–O clusters and reducing the outer steric hindrance of the polyoxotungstate. Similar structures were observed in **2Ln**. The tetrameric **3Gd** exhibited a Gd-shell@B-shell@Ni-shell@W-shell ({Gd_4}@{B_{22}}@{Ni_3}$_4$ @{B–SiW_9}$_4$) configuration featuring a cage-like 22-nuclearity Td-symmetry B–O cluster $[B_{22}O_{42}]^{18-}$ ({B_{22}}). This was the first observation of the {B_{22}} cluster topology in oxoboron cluster chemistry. Within the {B_{22}} cluster, six B_3O_7 three-rings are located in the tetrahedral arrays defined by four Gd^{3+} ions, forming a hollow tetrahedral cage $[Gd_4B_{22}O_{42}]^{6-}$ ({Gd_4}@{B_{22}}≡{Gd_4B_{22}}) with a diameter of approximately 1.2 nm through the connections of the Gd-and B-shells. A slightly larger tetrahedral cluster $[Ni_{12}Gd_4B_{22}O_{46}(OH)_{12}]^{6-}$ $\{Ni_{12}Gd_4B_{22}\}$ was formed by capping each corner of the tetrahedral $\{Gd_4B_{22}\}$ cage with three edge-shared NiO_6 octahedra ($Ni_3O(OH)_3$ core). Under the precondition of the isomerization from $\{A\text{-}SiW_9\}$ to $[B\text{-}\alpha\text{-}SiW_9O_{34}]^{10-}$ ($\{B–SiW_9\}$), four $\{B–SiW_9\}$ attached to four corners of $\{Ni_{12}Gd_4B_{22}\}$ cluster, resulting in the Td-symmetrical **3Gd**. **1Ln**, **2Ln**, and **3Ln** possessed 39, 21, and 24 protons, respectively, which were delocalized on the overall structures. All these POMs were soluble in water, but not in many solvents. **1Gd** was tested for the catalytic decontamination CEES, where it could selectively convert about 96 % of CEES into CEESO with 97 % selectivity in 2 h and a half-life of approximately 10 min. In a control experiment without **1Gd**, only around 66 % CEES was converted. Consistent IR and powder X-ray diffraction (PXRD) experimental results along with the maintained high activity of **1Gd** in six catalytic reactions confirmed its structural stability and recyclability.

Our group designed and synthesized a series of Ln-containing polytungstate ($[H_2N(CH_3)_2]_8Na_8Cs_4H_9$ $[Ln_2\text{-}SeW_4O_{11}(OH)(H_2O)_4(SbW_9O_{33})(SeW_9O_{33})(Se_{1/2}Sb_{1/2}W_9O_{33})]_2\cdot 32H_2O$ [Ln = Tb (**1**), Dy (**2**), Ho(**3**), Er (**4**)] (Figure 4)[56] and $Cs_{18}Na_8H_{20}$ $[Ce_3(H_2O)_{10}W_8Bi_4O_{28}(B\text{-}\alpha\text{-}BiW_9O_{33})_4]_2\cdot 64H_2O$ {SeO2 (OH)} (**5**)[57] for catalytic oxidation CEES. POMs **1**–**4** were in the monoclinic space group $P2_1/c$ and the hexameric architectures. In POMs **1**–**4**, two equivalent trimeric subunits $Ln_2W_4O_9(H_2O)_4(SbW_9O_{33})(SeW_9O_{33})(Se_{1/2}Sb_{1/2}W_9O_{33})$ were linked through two μ_2-$\{SeO_2(OH)\}$ bridges. Three different types of trivacant Keggin fragments $\{SbW_9\}$, $\{SeW_9\}$, and $\{Se_{1/2}Sb_{1/2}W_9\}$ were existed in compounds **1**–**4**, and $\{SeW_9\}$ was formed *in situ*, not from the raw materials. It was a rare occurrence that POM was constructed from different fragments with the central heteroatoms of trigonal pyramidal Sb^{III} and Se^{IV}. From the bond lengths of Se1/2Sb1/2–O located in the scope of 1.892–1.924, which were between that of Se–O and Sb–O bonds, indicating that 1/2 S b and 1/2 Se atoms co-occupied the central position of $Se_{1/2}Sb_{1/2}W_9O_{33}$ fragment. POM **three** was selected as a representative to investigate their catalytic oxidation ability of CEES. POM **three** exhibited that the remarkable oxidation activity of CEES with 99 % percent conversion of CEES into CEESO and a high selectivity of 95 % within 30 min. Without **3**, only 30 % conversion was observed. In addition, POM **three** exhibited a desirable heterogeneous catalytic behavior, and remained stable conversion and selectivity of CEES after five cycles. POM **five** was in monoclinic $C2/c$ space group and contained, and it was the first case that tungstobismuthate building blocks self-assembled into unprecedented octameric Ln-containing POM($[Ce_3(H_2O)_{10}W_8Bi_4O_{28}(B\text{-}\alpha\text{-}BiW_9O_{33})_4]_2^{46-}$) with an extended structure. The octameric $[Ce_3(H_2O)_{10}W_8Bi_4O_{28}(B\text{-}\alpha\text{-}BiW_9O_{33})_4]_2^{46-}$ was constructed by two tetrameric $[Ce_3(H_2O)_{10}W_8Bi_4O_{28}(B\text{-}\alpha\text{-}BiW_9O_{33})_4]^{23-}$ via two Ce–O–W bonds as linker, which was formed by a heterometallic cluster core $Ce_3(H_2O)_{10}W_8Bi_4O_{28}$ surrounded with four *B-α*-BiW9O33 fragments. POM **five** also demonstrated its.

brilliant catalytic oxidation performance of CEES. The conversion of CEES and selectivity to CEESO could reach 98 % and 96 % within 35 min, and the pseudo first-order dynamic reaction rate constant k_1 was 0.11632 min^{-1} with a

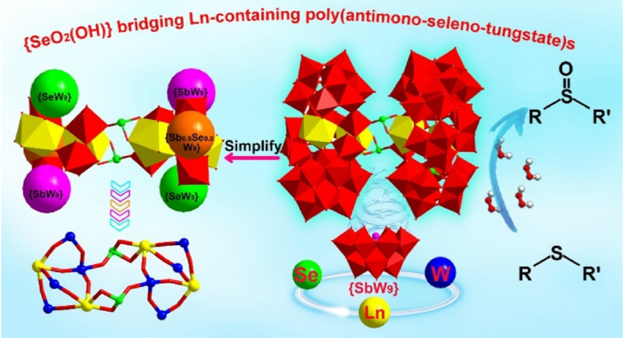

Figure 4: The crystal structures of ($[H_2N(CH_3)_2]_8Na_8Cs_4H_9$ $[Ln_2SeW_4O_{11}(OH)(H_2O)_4(SbW_9O_{33})(SeW_9O_{33})(Se_{1/2}Sb_{1/2}W_9O_{33})]_2\cdot 32H_2O$ [ln = Tb, dy, Ho, Er]. Reproduced with permission from ref. 56. Copyright 2021 American chemical Society.

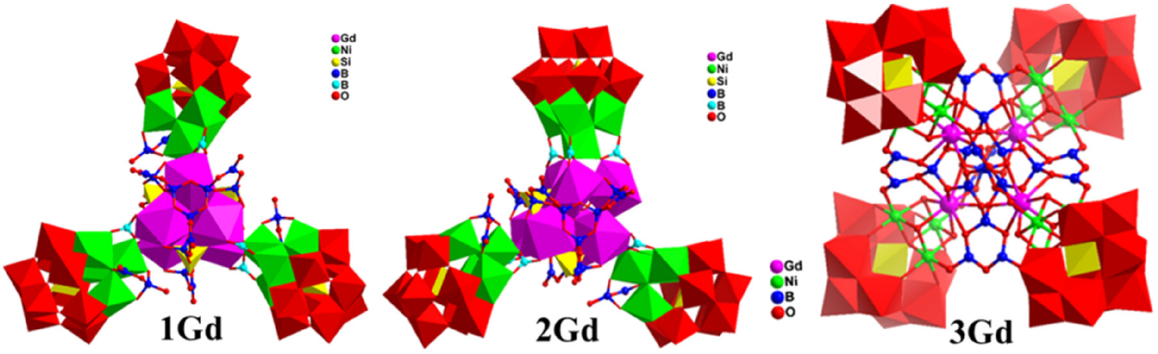

Figure 3: Crystal structures of POMs **1Gd**, **2Gd** and **3Gd.** Reproduced with permission from ref. 55. Copyright 2021 The Chinese chemical Society.

half-life of about 6 min. After five cycles, POM **five** still rrretained high catalytic activity and selectivity to CEESO, and meaning that POM **five** could be as a robust heterogeneous catalyst.

2.2 POMs-based MOFs for catalytic decontamination of vesicants

Liu's group designed two polyoxovanadate-based MOFs ([Co(bib)]{V_2O_6} (**V–Co-MOF**) and [Ni(en) (bib)]{V_2O_6}·$2H_2O$ (**V–Ni-MOF**) (bib = 1,4-bis(1H-imidazoly-1-yl)benzene, en = ethanediamine) for two-site synergetic catalytic decontamination of CEES.[58] One-dimensional (1D) {V_2O_6}$^{2-}$ polyanion chains (abbreviated as {V_2O_6}) were formed into two 2D bimetallic oxide layers, {CoV_2O_6} and {NiV_2O_6}, using {CoN_2O_2} tetrahedra and {NiN_4O_2} octahedra as linkers, and further assembled into 3D frameworks. The four-coordinated Co (II) ions in the **V–Co-MOF** were unsaturated metal sites, in contrast to the saturated six-coordinated Ni (II) ions of **V–Co-MOF**. The catalytic activities of both MOFs for CEES oxidation were studied. CEES was selectively oxidized to CEESO without 2-chloroethyl ethyl sulfone ($CEESO_2$) byproduct of. **V–Co-MOF** exhibited a higher catalytic activity than **V–Ni-MOF**. A pseudo-first order reaction of **V–Co-MOF** and **V–Ni-MOF** was deduced with the corresponding rate constants k_1 and k_2 of 0.27044 and 0.06273 min^{-1}, and the half-lives of 2.6 and 11.0 min, respectively. Through evaluating the catalytic activities of en, bib, $NiCl_2$, $CoCl_2$, NaK{V_2O_6}, NaK {V_2O_6} + $NiCl_2$, NaK{V_2O_6} + $CoCl_2$, **V–Ni-MOF** and **V–Co-MOF**, **V–Ni-MOF** possessed the highest catalytic activity, possibly owing to the generation of active peroxovanadium from the reaction of V^V with H_2O_2 and the CEES + via the coordination of Co(II) and S. **V–Co-MOF** could rapidly capture CEES with a maximum absorption of 14 mg g^{-1}, then activating CEES.[59] The binding energy of Co 2p in the XPS of CEES-absorbing **V–Co-MOF** showed a notable downward shift, indicating electron transfer from CEES to Co ions and a significant increase in electron density of Co ions in **V–Co-MOF**. Similar experimental results were observed with **V–Ni-MOF**. The formation of O–O in the peroxovanadium was verified by new peaks at 860 cm^{-1} and 870 cm^{-1} in the FTIR and Raman spectra. Throughout the reaction, the weight and structure of **V–Co-MOF** remained largely unchanged, demonstrating its high stability and recyclability. The possible mechanism was speculated based on the Experimental results and shown in Figure 5. This work was the first example of a dual-active-site POM-based MOF catalyst for mustard gas detoxification.

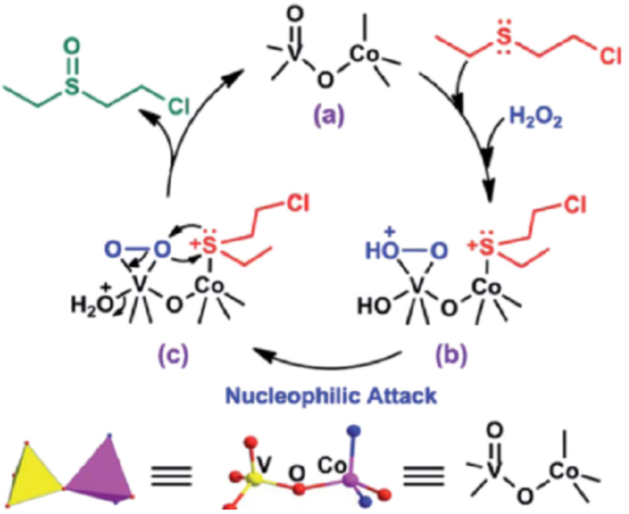

Figure 5: The proposed catalytic mechanism of CEES by V–Co-MOF. Reproduced with permission from ref. 58. Copyright 2020 The royal society of Chemistry.

Another POV-based MOF [Ni(bib)$_2$]{V_2O_6} (**{V_6}-MOF**) was successfully synthesized by Liu's group for the catalytic decontamination of CEES.[60] A hexanuclear vanadium anion cluster, {V_6O_{18}}$^{6-}$ ({V_6}) in **{V_6}-MOF** presented an unprecedented hollow Lindqvist-like structure compared with reported {V_6} clusters.[61] Bimetallic decanuclear cluster {Ni_4–V_6} was generated through the coordination between the {V_6} cluster and four Ni atoms. Through alternating {V_6} clusters and octahedral Ni atoms, a 2D bimetallic oxide layer of {$Ni_3V_6O_{18}$} emerged, which was further assembled into a 3D framework using bib ligand as the linker (Figure 6). **{V_6}-MOF** exhibited excellent thermal stability up to 450 °C and solvent stability, which was crucial to its sustainability. The catalytic activity of **{V_6}-MOF** on the oxidative detoxification of CEES was evaluated, whereby CEES was completely converted into nontoxic CEESO in 40 min with a half-life of 10.5 min. This was significantly faster than the 240 min reaction time of Lindqvist-type POV-based MOF catalyst also containing hexanuclear vanadium clusters, which was attributed to the more accessible V sites in **{V_6}-MOF {V_6}-MOF** compared to the Lindqvist-type {V_6} cluster. Feasible ratios of **{V_6}-MOF**: CEES and CEES: H_2O_2 was determined to be 0.05:1 and 1.0:1.2, respectively. Various raw materials and intermediates were used as catalysts in a series of control tests to verify the active components of **{V_6}-MOF**. {V_6}-mIM could completely catalyze the conversion of CEES to CEESO with 100 % selectivity, but bib and [$Ni^{II}(H_2O)_4(L)_2$] exhibited no activity, verifying that the main active site of **{V_6}-MOF** was the {V_6} cluster. A new Raman spectrum peak at 870 cm^{-1} assigned to the O–O stretch of **{V_6}-MOF** treated with H_2O_2 indicated the production of active peroxo species.

These species attacked S atom of CEES, generating nontoxic CEESO. The conversion and selectivity were retained after four successive runs. The consistent PXRD patterns, FTIR and XPS spectra of the cycled catalyst indicated that **{V$_6$}-MOF** could be applied as a highly effective catalyst for the detoxification of mustard gas due to its excellent stability and sustainability.

Liu's group developed a hollow POM@MOF with a pseudo-homoepitaxial structure $[Cu_2(BTC)_{4/3}(H_2O)_2]_6[H_3PW_{12}O_{40}]\cdot(C_4H_{12}N)_2$ (**NENU-3a**) for promoting the adsorption and catalytic performance toward CEES.[62] $H_3PW_{12}O_{40}$ (**PW$_{12}$**) as guest with ideal catalytic activity was perfectly encapsulated in the $[Cu_3BTC_2]$ (BTC = 1,3,5-benzenetricarboxylate) host through supramolecular assembly and formed, which exhibited a perfectly matched lattice/structure for $[Cu_3BTC_2]$ and **PW$_{12}$**, yielding desirable catalytic performance. Scanning electron microscopy (SEM) images of **NENU-3a** showed the clear transits from cuboctahedral to octahedral morphology, indicative of epitaxial growth. XRD patterns and FTIR peaks of **NENU-3a** confirmed the presence of $[Cu_3BTC_2]$ and **PW$_{12}$** in **NENU-3a**. Formation of an internal mesoporous structure was evident due to the noticeable interior collapse of the crystalline particle, leading to a clear hollow structure with a diameter of 700 nm after 1.5 min. Energy dispersive X-ray (EDX) elemental mapping revealed the distribution of Cu and W, confirming the hollow structure and the uniform epitaxial growth of **NENU-3a**. The stable existence of $[Cu_3BTC_2]$ in the **PW$_{12}$**/$Cu(NO_3)_2$ solution was attributed to the inhibition of **PW$_{12}$** dissociation in weak polar chloroform/methanol and lowering H^+ concentration. HNO_3, released from reactions between H_3BTC and $Cu(NO_3)_2$ in the **NENU-3a** assembly contributed to the formation of the hollow structure via in-diffusion etching. The concentration difference drove HNO_3 enriched in the confined space to diffuse inwardly through hydrogen bonding, etching the $[Cu_3(BTC)_2]$ cores. Without this, HNO_3 directly diffused to the exterior owing to the lack of hydrogen bonds, and relatively dilute HNO_3 could not etch the inside $[Cu_3(BTC)_2]$. Transmission electron microscopy (TEM) images and the concentration-dependent etching experiment of HNO_3 on $[Cu_3(BTC)_2]$ both confirmed the proposed internal diffusion mechanism in Figure 7. Etching occurred on the $[Cu_3(BTC)_2]$ surface only when the HNO_3 concentration increased to about 70 mM, which indicated that the interior was more readily etched than the exterior. Compared to $[Cu_3(BTC)_2]$ and solid **NENU-3a**, the intermediate Brunauer–Emmett–Teller (BET) surface area of hollow **NENU-3a** indicated that micropores were present only in the hollow layer of the surface, with some $[Cu_3(BTC)_2]$ remaining inside. Similar thermal stability was observed on hollow NENU-3a, mainly due to the stabilization and protective effect of its outer shell layers for the interior $[Cu_3(BTC)_2]$, in addition to its robust single-crystalline nature. Another POM@MOF ($[Cu_{12}(BTC)_8]$**[PMo$_{12}$]**) (**NENU-5a**) was constructed using the pseudo-homoepitaxial growth strategy, demonstrating the versatility of the strategy. The catalytic oxidation performance of CEES was tested on hollow **NENU-3a** with H_2O_2 as an oxidant. Hollow **NENU-3a** exhibited a faster catalytic rate than solid **NENU-3a**. The CEES conversions were almost 100 % and 86 % for hollow and solid **NENU-3a**, respectively, in 30 min. Moreover, hollow **NENU-3a** showed the higher selectivity toward CEESO than the solid form due to the rapid departure of CEESO from the shell structure, preventing over-oxidation. Hollow **NENU-3a** retained its catalytic activity, selectivity, morphology and cavity structure upon reuse.

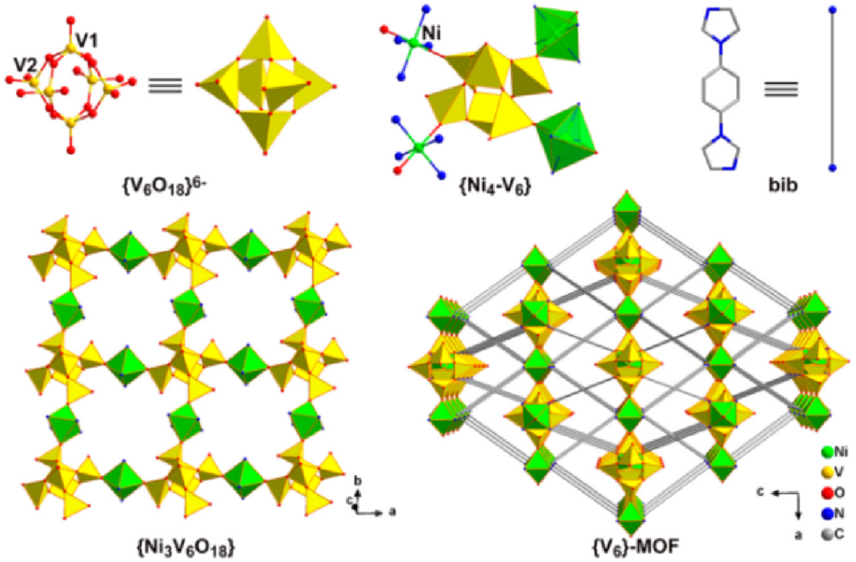

Figure 6: The crystal structure of {V$_6$}-MOF. Reproduced with permission from ref. 60. Copyright 2021 American chemical Society.

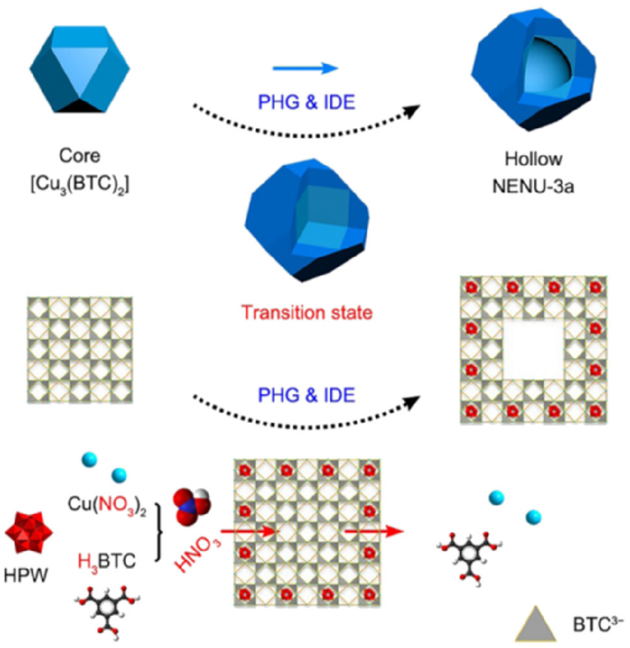

Figure 7: The proposed pseudo-homoepitaxial growth strategy of hollow POM@MOF. Reproduced with permission from ref. 62. Copyright 2022 Chinese chemical Society.

Wang's group synthesized a novel and multifunctional 2D POMOF $[Co^{II}(bcbpy)_2(\theta\text{-}Mo_8O_{26})_{0.5}]\cdot 5H_2O$ (**BHU-1**) through hydrothermal reactions of HbcbpyCl (1-(4-carboxybenzyl)-4,4′-bipyridinium chloride $[Mo_8O_{26}]^{4-}$, and Co^{2+}.[63] **BHU-1** was the first 2D $[\theta\text{-}Mo_8O_{26}]^{4-}$-based cobalt–viologen framework with a triclinic system and the space group P-1. The consistency of experimental and simulated PXRD confirmed the purity of **BHU-1**.[64] **BHU-1** exhibited two broad absorption bands, from 200 to 497 nm, and from 497 to 1,621 nm and one absorption peak at 1,663 nm, which were assigned to Mo–O ligand-to-metal charge transfer (LMCT), Co-bcbpy LMCT and the phenyl C–H stretching overtone band, respectively. Mott–Schottky (MS) electrochemical tests revealed that **BHU-1** was a typical n-type semiconductor with the Fermi level (E_f) of –1.15 eV versus Ag/AgCl. According to the valence band (VB)-XPS method, the gap between E_f and the VB potential of BHU-1 (0.73 eV, *vs.* NHS) was found to be 1.88 eV. Under visible light irradiation, Nyquist experiments indicated that **BHU-1** exhibited the fast separation and high transfer efficiency of photogenerated charge. **BHU-1** catalyzed the oxidation of 98 % of CEES with 97 % selectivity within 5 min in ethanol under visible light. Under full-spectrum and near-infrared (NIR) light irradiation, the conversions of CEES were 99 % and 93 %, respectively, and the selectivities were both 96 % within 5 min, which meant that the catalytic activity was retained under different light regimes. Using the raw materials as homogeneous catalysts, CEES conversions of 17 %, 21 %, and 18 % were achieved with $CoCl_2\cdot 6H_2O$, HbcbpyCl and $Na_2MoO_4\cdot 2H_2O$, respectively, indicating that the photocatalytic oxidation of CEES was enhanced by the synergy of the three components in **BHU-1**. The excellent cycling stability and durability was confirmed by recycling experiments and consistent PXRD and IR spectra. The catalytic reaction was simplified to a pseudo-first-order reaction using the Langmuir–Hinshelwood model.[65] The photogenerated electrons were separated from the hole with the help of C_2H_5OH in catalytic process of CEES, and the OH radical was easily produced through the reaction of H_2O_2 with photo-induced holes. The conversion rate of CEES was decreased by the introduction of BQ or tert-butyl alcohol (TBA), which indicated that CEES was oxidized to CEESO by O^{2-} and OH generated from the reaction between photogenerated electrons with oxygen. H_2O_2 could also facilitate O_2 circulation: $H_2O_2 + \cdot O_2^- \rightarrow O_2 + e^- \rightarrow O_2^- +$ CEES → peroxide intermediate + CEES → CEESO.

To leverage the complementary advantages of MOFs and POMs and achieve excellent catalytic performance, Zhou's group designed a composite material by encapsulating $H_5PV_2Mo_{10}O_{40}$ in MIL-101(Cr) for efficient CEES decontamination.[66] The *α*-Keggin $H_5PV_2Mo_{10}O_{40}$ showed promise for the amient decontamination of HD.[67] Using the impregnation method, the maximum loading amount of $H_5PV_2Mo_{10}O_{40}$ by MIL-101(Cr) was approximately 33.28 wt% even with additional $H_5PV_2Mo_{10}O_{40}$. Given the large 34 Å cages of MIL-101(Cr) and the diameter of 13 Å and volume of 2,250 $Å^3$ of $PV_2Mo_{10}O_{40}^{5-}$ anion, four $H_5PV_2Mo_{10}O_4$ per cage was speculated for the maximum loading sample. Analysis via IR spectra, XRD, TG, and N_2 adsorption/desorption experiments confirmed the successful preparation and intact crystalline structure of the MOF. Furthermore, the absence of characteristic peaks of $H_5PV_2Mo_{10}O_{40}$ in the XRD pattern of the composite and the elemental mapping analysis (Cr, O, P, Mo, and V) in the EDX spectra indicated a uniform distribution of $H_5PV_2Mo_{10}O_{40}$ in MIL-101(Cr). The maximum decontamination efficiency of CEES reached 90 % using 20 mg MIL-101(Cr). For the composite materials, the decontamination efficiency gradually increased with the loading amount of $H_5PV_2Mo_{10}O_{40}$ increasing. The maximum decontamination efficiency of HD was 97.39 % by the composite with the loading amount of 120 mg $H_5PV_2Mo_{10}O_{40}$. The decontamination reaction of HD exhibited pseudo-first order kinetics with a half-life of 26.38 min by theoretical fitting. Compared to $H_5PV_2Mo_{10}O_{40}$, MIL-101(Cr), or their physical mixtures, the composite showed superior performance, highlighting a synergetic effect. No products from the suspension in the decontamination process of MIL-101(Cr) were detected by gas chromatography/mass spectrometry (GC/

MS) except for CEES, implying the decontamination was adsorption. However, in the composite, CEES and CEESO were detected with the relative amounts of 64.93 % and 32.16 %, indicating a combined adsorption and oxidation degradation. Additionally, the composite outperformed activated clay, nano-Al_2O_3 and nano-MgO under the same conditions. Its decontamination efficiency remained at 93.83 % and its structure was intact even after four consecutive recycles using the composite. Notably, the negligible leakage of $H_5PV_2Mo_{10}O_{40}$ from MIL-101(Cr) in the recycle process was attributed to the insolubility of highly polar $H_5PV_2Mo_{10}O_{40}$ in nonpolar petroleum ether.

2.3 POMs composite for catalytic decontamination of vesicants

Three composites Zn_2Cr-LDH-$PW_{11}M(H_2O)O_{39}$ were constructed through exfoliation-reassembly of mono-transition metal (Ni, Co, Cu)–substituted POMs $[PW_{11}M(H_2O)O_{39}]^{5-}$ **($PW_{11}M$)** into layered double hydroxides (LDHs) **Zn_2Cr-LDH-NO_3** by Chi's group.[68] Increased in spacing layers (1.06 nm matching the diameter of cluster) observed in PXRD patterns of the composites indicated the replacement of small nitrate with large **$PW_{11}M$** and the intercalation of **$PW_{11}M$** into the LDH. Broad hump diffraction peaks (2θ = ~32-42°) and FTIR characteristic peaks of composites confirmed the preservation of the LDH lamellar structure and the integrity of POMs. SEM and TEM images showed that the intrinsic LDH nanosheet morphology retained in the composite. The loading amount of **$PW_{11}Ni$** was 52 wt% by inductively coupled plasma atomic emission spectroscopy (ICP-AES) analyses. Solid state ^{31}P NMR of composite **Zn_2Cr-LDH-$PW_{11}Ni(H_2O)O_{39}$** still exhibited the characteristic peak of $PW_{11}Ni$ (−11.3 ppm). The BET surface area and average pore size of composite **Zn_2Cr-LDH-$PW_{11}Ni(H_2O)O_{39}$** was enlarged to 24.92 m^2/g and 42.48 nm, respectively, from 13.56 m^2/g and 14.14 nm of the LDH host. CEES was used to evaluate the catalytic abilities of the composites, and **Zn_2Cr-LDH-$PW_{11}Ni$** exhibited the best catalytic performance with 98 % conversion. Similar selectivity (94 %) for nontoxic CEESO was observed for all three composites. At the same conditions, the catalytic conversions of CEES were 81 %, 78 %, 73 % and 30 % for **$PW_{11}Ni$**, **$PW_{11}Co$**, **$PW_{11}Cu$**, and **Zn_2Cr-LDH**, respectively, highlighting POM as the primary catalytic active species and the cooperative effect between POM and LDHs. The low conversions of 21 % and 58 % for plenary **PW_{12}** and lacunary $K_7PW_{11}O_{39}$, respectively, revealed the important roles of tungstophosphate and substituted transition metals in the catalytic reaction. The catalytic activity order of the composites was consistent with that of **$PW_{11}M$**. CEES conversion was increased with the amount of the composite **Zn_2Cr-LDH-$PW_{11}Ni$** and oxidant increasing. Initially, toxic $CEESO_2$ was formed within the first 30 min, and remained stable until the reaction was complete. **Zn_2Cr-LDH-$PW_{11}Ni$** maintained the good stability over nine cycles. Introducing several radical scavengers had no effect on the CEES conversion, indicating a non-radical reaction process for catalytic decontamination.

Due to the large accessible areas and workability of polymers with intrinsic microporosity (PIMs), Farha's group constructed PIM-based hybrid materials for CEES degradation using PIMs carriers for supporting POM ($H_3PW_{12}O_{40}$, **PW_{12}**) (Figure 8).[69] Three kinds of functionalized PIMs with cyano (**PIM-1**), carboxy (**PIM-1-COOH**) and amidoxime (**PIM-1-AO**) groups were prepared and used to evaluate their POM loading performances. The characteristic stretching vibration peaks of POM appearing in the FTIR spectrum of **PW_{12}@PIM-1-AO** were not observed in that of **PW_{12}@PIM-1** and **PW_{12}@PIM-1-COOH**, indicating that **PIM-1-AO** was a promising POM support. ICP-OES analysis indicated that about 80 % of POM was supported on **PIM-1-AO**, but only ~1 wt % on the others, revealing a strong interaction between POMs and **PIM-1-AO**. ^{31}P solid state NMR showed a chemical shift at −15.7 ppm, and ^1H NMR displayed –OH and –NH_2 shifts at 9.4 and 5.8 ppm, indicating the presence of free **PW_{12}** and interactions between POMs and the amidoxime of **PIM-1-AO**. The BET surface area of **PW_{12}@PIM-1-AO** decreased with the POM loading increasing. SEM images with EDX mapping confirmed uniform POM distribution in **PIM-1-AO**. Two XPS peaks of $4f_{7/2}$ and $4f_{5/2}$ at 36.3 and 38.5 eV in the W 4f region of **PW_{12}** were slightly shifted to lower binding energies for **PW_{12}@PIM-1-AO**. Combined with a broader peak at 399.8 eV in the *N* 1 s region and two O 1 s peaks at 532.8 and 530.1 eV, it was concluded that POMs were attached to **PIM-1-AO** via electrostatic interactions between the protonated amine groups and anionic POMs.[70] Uniform fibers with an average diameter of 1.2 µm were prepared from a mixed solution of POM and **PIM-1-AO** in DMF (40 % w/v) via the electro-spinning. Analyses of the ^{31}P cross-polarization magic-angle-spinning (CP/MAS) NMR spectrum, FTIR spectrum and EDX mappings of the composite fiber suggested that the POM was intact and uniform distributed within the fiber. **PW_{12}@PIM-1-AO** composite fibers exhibited complete catalytic conversion of CEES within 60 min with a selectivity of 86 % toward CEESO. However, full conversion of CEES by **PW_{12}@PIM-1-AO** composite powders required 90 min with 87 % selectivity toward CEESO. Compared with the full conversion and 95 % selectivity by homogeneous **PW_{12}** in 60 min, the trapping of CEESO in the pores of the composite possibly slightly reduced its selectivity. At the same conditions, negligible conversion of CEES occurred without an active catalyst or with **PIM-1-AO** fiber. The composite fibers with variable POM loading amounts could be prepared by immersing **PIM-1-AO** fibers into POM solution with different concentrations. Marginal conversion in the leaching tests further demonstrated the heterogeneous nature of the catalytic process. After three cycles, the conversion of CEES reached 72 ± 3.3 % after 60 min.

Wang's group designed a graphene supported polyoxotungstate $K_{1.5}Cs_{5.5}$ [γ-$SiW_{10}O_{39}Cu_2(N_3)_2$] (**$SiW_{10}Cu_2(N_3)_2$**) composite through a "click" reaction between the azido group of POM and the alkynyl groups on functionalized graphene, which boasted several advantages redox properties, higher thermal stability, electronic band structure, special hydrophobicity, and monodisperse sites (Figure 9).[71] Alkyne group-functionalized graphene (GO–C ≡ CH) was obtained through the reaction between graphene functionalized with a –COOH group and 4-(2-propynyloxy)aniline, which then reacted with **$SiW_{10}Cu_2(N_3)_2$** through a "click" reaction. The Raman spectrum of **$SiW_{10}Cu_2$/GO** with the peaks at 935 and 717 cm^{-1} confirmed the retention of the **$SiW_{10}Cu_2$** structure. XPS analysis of **$SiW_{10}Cu_2$/GO** showed binding energy peaks at ~935 and 932 eV corresponding to Cu^{2+} and Cu^{+}, respectively. This facilitated the electron transfer between graphene and **$SiW_{10}Cu_2$** and promoted the dismutation of H_2O_2 to O_2 and the oxidation reaction. TEM and EDX images of **$SiW_{10}Cu_2$/GO** revealed a single molecular layer of particles, approximately 1.2 nm in size (close to 10 Å of POMs) on the surface of **$SiW_{10}Cu_2$/GO** samples. **$SiW_{10}Cu_2$/GO** was used to catalyze the oxidation of CEES with H_2O_2. The conversion of CEES without **$SiW_{10}Cu_2$/GO** was 34.0 % with the selectivities of 50.9 % and 46.2 % toward CEESO and $CEESO_2$, respectively, after 60 min. A similar result was observed with the coexistence of graphene and H_2O_2. The addition of POM increased the conversion to 64.5 % with 100 % selectivity toward CEESO. The turnover frequency (TOF) increased from 0.748 min^{-1} for **$SiW_{10}Cu_2(N_3)_2$** to 51.556 for **$SiW_{10}Cu_2$/GO**. Under **$SiW_{10}Cu_2$/GO** catalysis, CEES was almost completely and selectively oxidized to CEESO. Radical scavenger experiments indicated no OH or superoxide free radicals in this catalytic system. The time-dependent absorbance decrease at 410 nm of 1,3-diphenylisobenzofuran (DPBF) (50 μM) with **$SiW_{10}Cu_2$/GO** catalyst (1 mg) and H_2O_2 (1.5 μM) indicated the emergence of singlet oxygen in this catalytic reaction. The CEES conversion of 72.0 % from the mixture of **$SiW_{10}Cu_2(N_3)_2$** and graphene after 60 min highlighted synergistic effects. Silence in the UV–vis band at 300–400 nm for **$SiW_{10}Cu_2(N_3)_2$** with H_2O_2 suggested that no peroxidation occurred, except for H_2O_2 dismutation. A decomposition efficiency of 35.9 % at 5 min and 61.5 % at 30 min for H_2O_2 on **$SiW_{10}Cu_2$/GO** was observed, with a decomposition rate of 1.35×10^{-1} μmol s^{-1} for H_2O_2, exceeding the 1.89×10^{-2} μmol s^{-1} rate of **$SiW_{10}Cu_2(N_3)_2$** at 30 min. This efficiency benefited from $SiW_{10}Cu_2$ being bonded as single molecules to the graphene surface, unlike the assembly of **$SiW_{10}Cu_2(N_3)_2$**. XPS result revealed that the molar ratio of Cu^{2+} and Cu^{+} in **$SiW_{10}Cu_2$/GO** was 1.3:1, which possibly enhanced the dismutation of H_2O_2 to O_2. A slightly higher reaction rate for heterogeneous CuCl compared to $CuCl_2$ indicated a higher activity for Cu^{+}. **$SiW_{10}Cu_2(N_3)_2$** achieved a 48.1 % conversion of CEES at 6 h through aerobic oxidation. For **$SiW_{10}Cu_2$/GO**, the conversion of CEES was significantly increased with increasing concentrations of O_2 and CEES around the graphene interface. The adsorption amount of **$SiW_{10}Cu_2$/GO** for CEES and O_2 was much larger than that of **$SiW_{10}Cu_2(N_3)_2$**. The hydrophobic environment of **$SiW_{10}Cu_2$/GO** readily adsorbed more oleophilic molecules, but not polar molecules. When oleophilic CEES was.

oxidized to polar CEESO, CEESO was repelled and escaped from **$SiW_{10}Cu_2$/GO**, preventing peroxidation to $CEESO_2$, as confirmed by XPS and IR experiments. Electron transfer and synergistic effects between **$SiW_{10}Cu_2$** and graphene promoted the aerobic oxidation of CEES. A selectivity of 100 % toward CEESO was still achieved with physically mixed hybrid **$SiW_{10}Cu_2(N_3)_2$/GO,** although the conversion was only 49.0 % at 6 h.[72] Near-perfect CEES conversion and minimal leaching were observed after 10 cycles of **$SiW_{10}Cu_2(N_3)_2$/GO**. The maintained structure and morphology confirmed by IR, ^{29}Si MAS NMR, XPS and TEM images of **$SiW_{10}Cu_2$/GO** after the cycle experiment

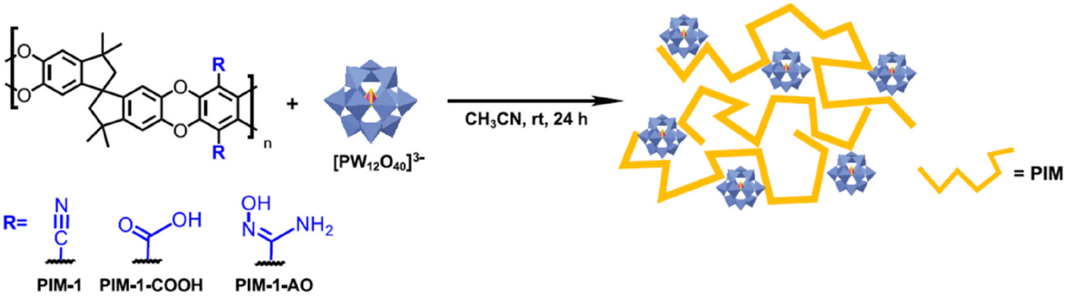

Figure 8: The synthesis routine of PIM-based composite. Reproduced with permission from ref. 69. Copyright 2022 American chemical Society.

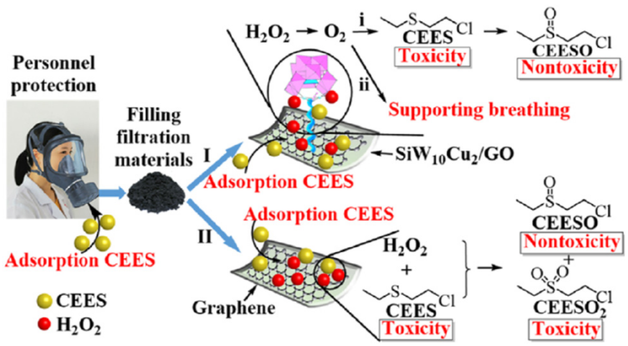

Figure 9: The schematic diagram of simultaneous dismutation of H_2O_2 to O_2 and oxidation of CEES by $SiW_{10}Cu_2$/GO catalyst. Reproduced with permission from ref. 71. Copyright 2020 American chemical Society.

demonstrated its potential as a catalyst for mustard gas analogue removal via aerobic oxidation at room temperature without additives.

Farha's group prepared a composite material **PW_{12}@NU-1000** via the direct impregnation method for catalytic oxidation of CEES leveraging the advantages of MOF NU-1000 and POM $H_3PW_{12}O_{40}$ (**PW_{12}**), such as small triangular channels (12 Å) and larger hexagonal channels (31 Å) for fast substrate diffusion, the suitable size and high catalytic activity.[73] About 0.8 $[PW_{12}O_{40}]^{3-}$ was loaded per Zr_6 node in NU–1000 as confirmed by ICP-OES. SEM images with EDS mapping showed the intact size and morphology of NU-1000 and the uniform dispersion of **PW_{12}** within the MOF, not just on the surface. Compared to bare NU-1000, the BET surface area and the length of the large hexagonal pores of **PW_{12}@NU-1000** were greatly decreased from 2,100 m^2/g and 31 Å to 850 m^2/g and 25 Å, respectively. The absence of non-H bonded–OH and H_2O characteristic peaks on the NU-1000 node and the presence of H-bonded H_2O and–OH peaks in diffuse reflectance infrared fourier-transform spectroscopy (DRIFTS) of **PW_{12}@NU-1000** indicated that the non-H-bonded H_2O and hydroxyl ligands were replaced by POM. **PW_{12}@NU-1000** exhibited good stability in HCl solution (pH 2–7) and only a 13 % loss of POMs after one week at pH 6, with less lost at lower pH values. **PW_{12}@NU-1000** effectively catalyzed the oxidation of CEES with a TOF of 10.4 min^{-1} in acetonitrile (1 mL) at 45 °C. In contrast, **PW_{12}** and NU-1000 alone had lower TOFs of 9.3 and 3.1 min^{-1}, respectively. For instance, full conversion of CEES was obtained by **PW_{12}** within 90 min, whereas **PW_{12}@NU-1000** needed only 20 min under the same conditions. The cooperative effect between the POM and MOF endowed **PW_{12}@NU-1000** with a faster initial rate and higher conversion efficiency than either component alone. However, the selectivity of **PW_{12}** to CEESO was superior to that of **PW_{12}@NU-1000**. The 10 % conversion and absence of a phosphorous NMR signal after the filtration of **PW_{12}@NU-1000** suggested negligible leaching of POMs from the MOF during catalysis. The selectivity and reactivity were maintained upon recycling under these catalytic conditions, and the integrity of the composite material was unchanged in the cyclic catalytic process.

Farha's group synthesized **PW_{12}@NU-1000-scCO_2** and **PW_{12}@NU-1000-120°C** by the incorporation of $H_3PW_{12}O4_0$ (**PW_{12}**) into the MOF, NU-1000, and the influence of the POM on catalytic performance was studied.[74] **PW_{12}@NU-1000-scCO_2** was obtained via activation by supercritical CO_2 drying, and **PW_{12}@NU-1000-120°C** was synthesized in 120 °C oven for over 1 h. ICP-OES analysis indicated a maximum loading of 0.8 POMs per Zr_6 node in both composites, with near uniform **PW_{12}** distribution (Figure 10). *In situ* variable temperature PXRD patterns showed that **PW_{12}@NU-1000-scCO_2** was changed into **PW_{12}@NU-1000-120°C** via heating to and maintaining at 120 °C, and the process was not reversible. Through differential envelope density (DED) analyses, POMs of **PW_{12}@NU-1000-scCO_2** were located in the hexagonal mesoporous channels, as opposed to the triangular microporous channels of **PW_{12}@NU-1000-120°C**. N_2 adsorption isotherms and DFT results indicated a reduction in mesopore volume for PW_{12}@NU-1000-scCO_2 and micropore volume for **PW_{12}@NU-1000-120°C**, with the BET surface area decreasing from 1,020 $m^2\,cm^{-3}$ to 700, and 850 $m^2\,cm^{-3}$, respectively. The difference in BET was due to 5 wt% water present during the activated process of **PW_{12}@NU-1000-scCO_2**. At 170 °C, and a slight exothermic change in the differential scanning calorimetry (DSC) curve of **PW_{12}@NU-1000-scCO_2** indicated the loss of water H-bonded to the acidic protons of **PW_{12}@NU-1000-scCO_2**, correlating to POM movement from mesopore to micropore under the increasing van der Waals forces. In the micropore, POM was encircled by three pyrene linkers, as opposed to one pyrene linker in the mesopore. The broader and shifted of ^{31}P signal indicated the loss of phosphorous symmetry and that POM strongly interacted with the MOF. The shift of reduction events to more positive potentials in the cyclic voltammograms (CVs) of **PW_{12}@NU-1000-120°C** from $H_3PW_{12}O_{40}$ also indicated a stronger interaction between **PW_{12}** and pyrene, making it more easily reducible than POM alone. Fluorescence quenching of bare NU-1000 by POM about 95–99 % indicated the electron transfer from pyrene linkers to POM. Catalytic oxidation of CEES to CEESO was used to evaluate the catalytic performance of both composites. The half-lifes of catalytic oxidation of CEES were 13, 5, 3, and 1 min for NU-1000, **PW_{12}**, **PW_{12}@NU-1000-120°C**, and **PW_{12}@NU-1000-scCO_2**, respectively. The selectivity of **PW_{12}@NU-1000-scCO_2** toward CEESO was 90.5 %, which was higher than that of **PW_{12}@NU-1000-120°C** (59 ± 7 %). Similar to its selectivity toward CEESO, the TOF of **PW$_{12}$@NU-1000-scCO$_2$** was about three times that of **PW$_{12}$@NU-1000-120°C**. POMs situated in the mesopores facilitated sulfide diffusion to POM and the near-exclusive generation of singly-oxidized product. Leach tests confirmed the heterogeneity of the reaction and the stability of POMs in the composite during catalysis.

Compared with **PW$_{12}$@NU-1000**, **PV$_2$Mo$_{10}$@NU-1000** was designed for catalytic degradation of CEES through immobilising decamolybdodivanado phosphoric acid ($H_5PV_2Mo_{10}O_{40}$, **PV$_2$Mo$_{10}$**) in NU-1000.[75] ICP-OES revealed a loading of 1.3 **PV$_2$Mo$_{10}$** per Zr_6 node. SEM images and EDS scans showed that the NU-1000 crystallite was retained, with POM homogeneously distributed throughout the crystallite. The BET surface areas of **PV$_2$Mo$_{10}$@ NU-1000-scCO$_2$** and **PV$_2$Mo$_{10}$@NU-1000-80 °C** slightly increased to 1,160 and 1,190 $m^2\ cm^{-3}$ from the original 1,020 $m^2\ cm^{-3}$ of NU-1000. The mesoporous peak was reduced and the microporous peak was retained for **PV$_2$Mo$_{10}$@NU-1000-scCO$_2$**. The opposite phenomenon was observed for **PV$_2$Mo$_{10}$@NU -1,000-80 °C**. These results suggested that POMs were located in the mesopores of **PV$_2$Mo$_{10}$@NU -1000-scCO$_2$** and in the micropores of **PV$_2$Mo$_{10}$@NU-1000-80 °C**, which was verified by comparison of PXRD pattern of NU-1000 and **PV$_2$Mo$_{10}$@NU-1000-scCO$_2$**.[76] *In situ* temperature-dependent PXRD experiments revealed that POM migration from mesopores to micropores occurred earlier in **PV$_2$Mo$_{10}$@NU-1000-scCO$_2$** than in **PW$_{12}$@NU-1000**. The ^{31}P NMR spectra of both composites broadened with slight shifts, indicating slight distortion of POM due to its interaction with the MOF framework. Compared to **PMo$_{12}$@NU-1000**, vanadium atoms were found to play a crucial role in aerobic activity, consistent with previous reports.[73] CEESO$_2$ was almost the only product even after CEES consumption. Despite optimising the reaction conditions, over-oxidized CEESO$_2$ was still formed and the reaction rate was severely decreased. Although approximately 20 % POM leached from both composites, 100 % CEES conversion by **PV$_2$Mo$_{10}$@NU-1000** was achievable in a second catalytic trial. In contrast, 5 % conversion was obtained using recycled $H_5PV_2Mo_{10}O_{40}$ due to POM decomposition. The *in situ* PXRD patterns of the composite, either as a dry powder or as a suspension in cyclohexane, indicated that solvent molecules could hinder migration of POM from mesopore to micropore. The MOF support strengthened the stability of POM in the composite.

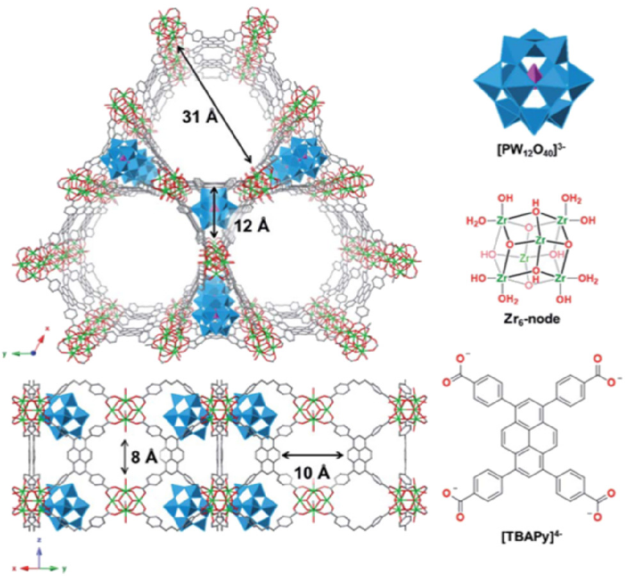

Figure 10: Visual structures of PW$_{12}$@NU-1000-scCO$_2$ and PW$_{12}$@NU-1000-120 °C. Reproduced with permission from ref. 74. Copyright 2018 The royal society of Chemistry.

An's group designed two novel POMOFs $\{[\varepsilon\text{-PMo}_8\text{-}{}^{\text{VMo}}{}_4{}^{\text{VI}}\text{O}_{37}(\text{OH})_3][\text{Zn}_2(\text{C}_{10}N_2\text{H}_8)\ (\text{H}_2\text{–O})_2]_2\}_2\cdot 8\text{H}_2\text{O}$ (**PMo$_{12}$O$_{37}$Zn$_4$-*α*** and **PMo$_{12}$O$_{37}$Zn$_4$-*β***) for the selective catalytic oxidation of multitudinous sulfides in which POMs was well dispersed at the molecular level and more active sites were exposed.[77] **PMo$_{12}$O$_{37}$Zn$_4$-*α*** and **PMo$_{12}$O$_{37}$Zn$_4$-*β*** were prepared at a pH = 5.3 ± 0.1 and 4.7 ± 0.1, respectively, containing four Mo^{V} and two Mo^{VI} in the asymmetric unit. One-dimensional inorganic chains were initially formed by linking one hexacoordinated Zn_4-ε-Keggin POM unit with two adjacent Zn_4-ε-Keggin POM units perpendicular to the ab plane, creating a 3D framework through coordination with bpy ligands along the c axis, parallel to the ab plane. The difference between **PMo$_{12}$O$_{37}$Zn$_4$-*α*** and **PMo$_{12}$O$_{37}$Zn$_4$-*β*** was the rotation of approximately 39° clockwise acround the b axis. The XPS spectra differences for P 2p and Zn 2p in **PMo$_{12}$O$_{37}$Zn$_4$-*α*** and **PMo$_{12}$O$_{37}$Zn$_4$-*β*** indicated that P^{5+} and Zn^{+2} were in two distinct POMs. According to the deconvolution of the spectra, the ratio of Mo^{V}/Mo^{VI} was approximately 2:1 for POMOFs **PMo$_{12}$O$_{37}$Zn$_4$-*α*** and **PMo$_{12}$O$_{37}$Zn$_4$-*β***. The broad absorption band at 400–800 nm indicated the electronic transition of reduced molybdenum ions. **PMo$_{12}$O$_{37}$Zn$_4$-*α*** and **PMo$_{12}$O$_{37}$Zn$_4$-*β*** were used as heterogeneous catalysts in the catalytic oxidation of CEES. Both exhibited outstanding catalytic oxidation performance of CEES under conditions of $n_{CEES}/n_{pre\text{-}catalyst}/n_{oxidant}$ = 1:0.005:1.08, at room temperature, in 0.5 mL of methanol. Over 99 % of CEES was oxidized into CEESO with more than 99 % selectivity by **PMo$_{12}$O$_{37}$Zn$_4$-*α*** in 15 min and **PMo$_{12}$O$_{37}$Zn$_4$-*β*** in 18 min (Figure 11). The catalytic efficiency decreased slifhtly after four consecutive trials. The structure remained unchanged before and after the catalytic reaction, demonstrating remarkable stability and recyclability. The catalytic oxidation reactions showed quasi-first order kinetics, with kinetic constants of 0.1561 and 0.2484 min^{-1} for **PMo$_{12}$O$_{37}$Zn$_4$-*α*** and **PMo$_{12}$O$_{37}$Zn$_4$-*β***, respectively. The synergistic effect of the raw materials along with their unique structure significantly contributed to the excellent catalytic activity and stability. The appearance of a new absorption peak at 237 nm and Raman spectrum peak at 760 cm^{-1} of a **$PMo_{12}O_{37}Zn_4$-*α*** solution treated with H_2O_2 assigned to O–O stretching indicated the formation of peroxo species in the catalytic process, which attacked the electron-rich S atom of the sulfide to produce the target product. The addition of multiple scavengers did not effectively prevent the oxidation reaction, further confirming the generation of peroxo species in the catalytic process.

Yang's group designed four polyoxomolybdate-based inorganic–organic hybrid materials for the catalytic oxidation of HD stimulant $[Mn\ (TMR4A)\ (H_2O)_4][Mo_6O_{19}]\cdot 0.5CH_3CH_2OHH_2O$ $[Ni(TMR4A)\ (H_2O)_4][Mo_{6\_}O_{19}]\cdot 0.5CH_3CH_2OHH_2O$ $[Zn\ (TMR4A)\ (H_2O)_4][Mo_6O_{19}]\cdot 0.5CH_3CH_2OHH_2O$, and $Co_2(TMR4A)_2(H_2O)_4\ (\beta–Mo_8O_{26})]\cdot CH_3CN\cdot 12H_2O$ using a self-assembly strategy (Figure 10).[78] Synthesis in different solvents, these hybrids exhibited distinct crystal structures. The first three samples contained $[Mo_6O_{19}]^{2-}$ anions and the last one contained $[\beta\text{-}Mo_8O_{26}]^{4-}$ anions. All four materials remained stable in various organic solvents and H_2O (pH = 0–12) for 12 h. Without catalyst, only 12 % of CEES was converted to CEESO and $CEESO_2$ at 40 °C for 25 min, using 0.25 mmol CEES, 4 ml CH_3OH and 1 mmol H_2O_2. With the addition of $[Mn\ (TMR4A)\ (H_2O)_4][Mo_6–O_{19}]\cdot 0.5CH_3CH_2OHH_2O$ (1.25 μM), the conversions of CEES could reach 93 %and 99 % with 97 % selectivity at 30 and 40 °C, respectively, after 25 min, demonstrating its superiority as a catalyst for CEES. No catalytic activity was observed after filtering the catalyst, and the absence of Mn^{II} cations in the filtrate indicated a heterogeneous reaction. FTIR spectra and PXRD patterns of the catalyst after four cycles confirmed its structural integrity. Catalytic experiments using multiple components indicated that polyoxomolybdate was the primary catalytic active site.

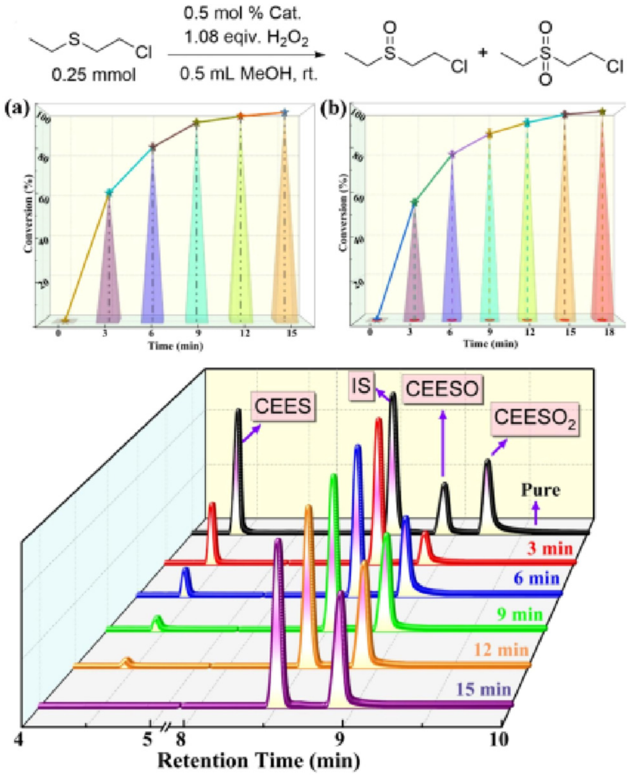

Figure 11: The catalytic performance of CEES by **$PMo_{12}O_{37}Zn_4$-*α*** (a) and **$PMo_{12}O_{37}Zn_4$-*β*** (b). Reproduced with permission from ref. 77. Copyright 2021 American chemical Society.

Jiao's group fabricated four nylon-6/POMs composite nanofibrous membranes ($H_3PW_{12}O_{40}\cdot xH_2O$, $H_4PMo_{11}VO_{40}\cdot xH_2O$, $H_5PMo_{10}V_2O_{40}\cdot xH_2O$ and $H_6PMo_9V_3O_{40}\cdot xH_2O$, abbreviated as **nylon-6/PW**, **PMoV1**, **PMoV2** and **PMoV3**) by electrospinning.[79] FTIR absorption peaks at 1,080–1,060 cm^{-1}, ca. 960 cm^{-1}, and 860–900 cm^{-1}, 780 cm^{-1} assigned to the corresponding stretching vibrations of P–O, Mo=O and Mo–O–Mo bonds, confirmed the successful preparation of **PMoV1**, **PMoV2** and **PMoV3**. SEM images showed that the diameter of **nylon-6/PW** nanofibers was 500–700 nm, whereas that of **nylon-6/PMoV1**, **nylon-6/PMoV2** and **nylon-6/PMoV3** nanofibers ranged from 50 to 100 nm. The higher viscosity of nylon-6/PW precursor solution led to the larger fibers. The nylon-6/POMs membranes exhibited decent thermal stability below 200 °C. Compared with the other composite membranes, **nylon-6/PMoV3** exhibited the highest HD degradation rate, which was 41.55 % in 6 h. Increasing the V content in POMs was beneficial for redox catalysis and resulted in the appearance of more reactive lattice oxygen associated with the Mo–O–V species. For **nylon-6/PMoV1**, the relative lower degradation efficiency was attributed to reduced mobility due to water loss. Considering the aerosol form of HD at ambient conditions, the filtration behaviors of these composite membranes were evaluated. Using **nylon-6/PMoV3** as a typical example and PP nonwoven fabric as a support the aerosol filtration efficiency increased significantly to 98.35 % in 3 h, much greater than that of PP nonwoven fabric alone (11.45 %). The mass per square meter of the **nylon-6/PMoV3** fibrous membrane was about 2.6 times that used in typical HD degradation experiments. Most HD was blocked by the membrane, and penetrating HD was rapidly degraded, indicating the potential of these composite nanofibrous membranes in soft protecting materials for *in situ* degradation of HD.

Babri's group prepared $H_3PW_{12}O_{40}/TiO_2$ and $H_6P_2W_{16}O_{62}/TiO_2$ via a sol-gel technique for photocatalytic degradation of HD.[80] To understand solvent effect, photocatalytic oxidation of HD by illuminated TiO_2 (150 mg) was investigated in relatively low viscosity solvents: hexane, acetonitrile, and acetone. After 90 min of irradiation, degradation rates of HD in the above solvents were 95 %, 90 %, and 88 %, respectively. The lower degradation rates in acetonitrile and acetone were due to reduced adsorption of the agent on TiO_2 surfaces, caused by the good solubility of HD in these solvents. Photocatalytic degradation of HD by POMs/TiO_2 was carried out in hexane because the physically adsorbed HD on the nTiO_2 surface could not be completely washed by hexane and hexane was inert and transparent. However, POMs/TiO_2 did not exhibit the ideal photocatalytic decontamination efficiency toward HD, indicating that POMs embedded in TiO_2 did not significantly enhance the catalytic effect. Under no radiation filtering, HD was possibly photolysed by the radiation. By only UV irradiation, the decontamination efficiency of HD could reach to 90 % via direct photolysis in 360 min. However, nearly 95 % HD was eliminated by nanoTiO_2 in 90 min. GC-MS analysis revealed that sulfoxide was initially formed, followed by sulfone, and elimination reactions occurred on both oxidation products, producing monovinyl and divinyl sulfoxides and sulfones. During photocatalytic degradation, no products or intermediates were detected, suggesting that the degradation products were adsorbed on the TiO_2 surface. These products were detected when acetone was used as the extracting solvent for the TiO_2 surface. Due to the presence of hydroxyl groups on the surface of nanoTiO_2, hydrolytic reactions still occurred, but the incomplete hydrolysis products were less toxic than HD itself.

3 Conclusions

We summarized the recent advances in POM-based catalysts for removal of vesicants in the last decade. These POM-based catalysts exhibited the outstanding catalytic performance to vesicants benefited from their tunable solubility, high thermal and redox stability, variable valences of metals, and Lewis base and acidity properties. The synergistic effect of valence states inter-conversion of metals and the doping of other metal ions enhance intermolecular electron transfer, that is salutary to oxidate removal of vesicants. Additionally, the dual-anion POMs can possess multifunctional catalytic capacities for different kinds of CWAs. Up to now, it is the greatest challenge to POM-based catalysts is catalytic oxidation decontamination of vesicants without H_2O_2. Hence, it may be the future development direction to design high active POM-based catalysts, that can selectively oxidate vesicants only depending on oxygen in the air. On the other hand, the combination of the wearable fabric and POM-based catalysts is necessary to subsequent practical application.

Research ethics: Not applicable.
Informed consent: Not applicable.
Author contributions: Aiping Gao: Writing–original draft. Si-Han Zhao and Jiajia Wang: Investigation. Hai-Lou Li: Supervision, Writing–review & editing. All authors approved the final manuscript.
Use of Large Language Models, AI and Machine Learning Tools: None declared.
Conflict of interest: All other authors state no conflict of interest.
Research funding: The authors declare no conflict of interest, financial or otherwise, that could influence the research findings or interpretation presented in this review.
Data availability: Not applicable.
Copyright and Permissions: Figures/tables reproduced from prior publications are duly credited with permission from the original copyright holders (if applicable).

References

1. DeCoste, J. B.; Peterson, G. W. *Chem. Rev.* **2014**, *111*, 5695–5727.
2. Kumar, V.; Rana, H.; Raviraju, G.; Gupta, A. K. Chemo Dosimeter for Selective and Sensitive Chromogenic and Fluorogenic Detection of Mustard Gas for Real Time Analysis. *Anal. Chem.* **2018**, *90*, 1417–1422.
3. Saladi, R. N.; Smith, E.; Persaud, A. N. Mustard: a Potential Agent of Chemical Warfare and Terrorism. *Clin. Exp. Dermatol.* **2006**, *31*, 1–5.
4. Baršienė, M. H.; Karjalainen, M.; Niemikoski, H.; Vanninen, P.; Broeg, K.; Lehtonen, K. K.; Berglind, R.; Baršienė, J. Toxic Effects of Chemical Warfare Agent Mixtures on the Mussel *Mytilus Trossulus* in the Baltic Sea: a Laboratory Exposure Study. *Mar. Environ. Res.* **2019**, *145*, 112–122.
5. Smith, B. M. Catalytic Methods for the Destruction of Chemical Warfare Agents Under Ambient Conditions. *Chem. Soc. Rev.* **2008**, *37*, 470–478.
6. Szinicz, L. History of Chemical and Biological Warfare Agents. *Toxicology* **2005**, *214*, 167–181.
7. DeCoste, J. B.; Peterson, G. W. Metal–Organic Frameworks for Air Purification of Toxic Chemicals. *Chem. Rev.* **2014**, *114*, 5695–5727.
8. Ko, Y.; Bae, E. J.; Chitale, S. K.; Soares, C. V.; Leitão, A. A.; Kim, M.-K.; Chang, J.-S.; Maurin, G.; Ryu, S. G.; Lee, U.-H. *ACS Appl. Nano Mater.* **2022**, *5*, 9657–9665.
9. Das, N.; Paul, R.; Tomar, S.; Biswas, C.; Chakraborty, S.; Mondal, J. Catching an Oxo Vanadate Porous Acetylacetonate Covalent Adaptive Catalytic Network that Renders Mustard-Gas Simulant Harmless. *Inorg. Chem.* **2024**, *63*, 6092–6102.
10. Weetman, C.; Notman, S.; Arnold, P. L. Destruction of Chemical Warfare Agent Simulants by Air and Moisture Stable Metal NHC Complexes. *Dalton Trans.* **2018**, *47*, 2568–2574.
11. Meng, Y.; Luo, Y.; Shi, J.-L.; Ding, H.; Lang, X.; Chen, W.; Zheng, A.; Sun, J.; Wang, C. 2D and 3D Porphyrinic Covalent Organic Frameworks: the Influence of Dimensionality on Functionality. *Angew. Chem., Int. Ed.* **2020**, *59*, 3624–3629.
12. Wu, B.; Liu, Y.; Zhang, Y.; Fan, L.; Li, Q.-Y.; Yu, Z.; Zhao, X.; Zheng, Y.-C.; Wang, X.-J. Molecular Engineering of Covalent Triazine Frameworks for Highly Enhanced Photocatalytic Aerobic Oxidation of Sulfides. *J. Mater. Chem. A* **2022**, *10*, 12489–12496.
13. Sheng, W.; Shi, J.-L.; Hao, H.; Li, X.; Lang, X. Selective Aerobic Oxidation of Sulfides by Cooperative polyimide-Titanium Dioxide Photocatalysis and Triethylamine Catalysis. *J. Colloid Interface Sci.* **2020**, *565*, 614–622.

14. Meng, Q.; Doetschman, D. C.; Rizos, A. K.; Lee, M.-H.; Schulte, J. T.; Spyros, A.; Kanyi, C. W. Adsorption of Organophosphates Into Microporous and Mesoporous Nax Zeolites and Subsequent Chemistry. *Environ. Sci. Technol.* **2011**, *45*, 3000–3005.
15. Aubert, S. D.; Li, Y.; Raushel, F. M. Mechanism for the Hydrolysis of Organophosphates by the Bacterial Phosphotriesterase. *Biochemistry* **2004**, *43*, 5707–5715.
16. Wagner, G. W. Nanoscale Materials in Chemistry. *Environ. Appl.* **2010**, 125–136, Chapter 7.
17. Oheix, E.; Gravel, E.; Doris, E. Catalytic Processes for the Neutralization of Sulfur Mustard. *Chem. Eur J.* **2021**, *27*, 54–68.
18. Pope, M. T. *Heteropoly and Isopoly Oxometalates*; Springer-Verlag: Berlin, 1983; pp 26.
19. Wang, S.-S.; Yang, G.-Y. Recent Advances in Polyoxometalate-Catalyzed Reactions. *Chem. Rev.* **2015**, *115*, 4893–4962.
20. Anyushin, A. V.; Kondinski, A.; Parac-Vogt, T. N. Hybrid Polyoxometalates as Post-Functionalization Platforms: from Fundamentals to Emerging Applications. *Chem. Soc. Rev.* **2020**, *49*, 382–432.
21. Ma, T.; Yan, R.; Wu, X.; Wang, M.; Yin, B.; Li, S.; Cheng, C.; Thomas, A. Polyoxometalate-Structured Materials: Molecular Fundamentals and Electrocatalytic Roles in Energy Conversion. *Adv. Mater.* **2024**, *36*, 2310283.
22. Fabre, B.; Falaise, C.; Cadot, E. Polyoxometalates-Functionalized Electrodes for (Photo)Electrocatalytic Applications: Recent Advances and Prospects. *ACS Catal.* **2022**, *12*, 12055–12091.
23. Cui, L.-M.; Fang, W.-H.; Zhang, J. Polyoxometalates Containing Aluminum Atoms. *Chin. Chem. Lett.* **2024**, 110386. https://doi.org/10.1016/j.cclet.2024.110386.
24. Li, K.; Liu, T.; Ying, J.; Tian, A.; Wang, X. Recent Research Progress on Polyoxometalate-Based Electrocatalysts in Energy Generation. *J. Mater. Chem. A* **2024**, *12*, 13576–13604.
25. Wang, Y.; Yu, Z.; Xiong, J.; Yan, K.; Lu, X. Temperature-Responsive Polyoxometalates-Based Materials: From Underlying Mechanism to Promising Applications. *Adv. Func. Mater.* **2024**, *34*, 2405880.
26. Ma, X.-Q.; Xiao, H.-P.; Chen, Y.; Lai, Q.-S.; Li, X.-X.; Zheng, S.-T. Polyoxometalate-Based Macrocycles and Their Assembly. *Coord. Chem. Rev.* **2024**, *510*, 215818.
27. Liu, R.-L.; Chen, Y.; Su, X.; Zhu, W.; Liu, Z.; Chen, Y.; Wang, D.-Y.; Li, G. Proton Conductive Polyoxometalates. *Coord. Chem. Rev.* **2025**, *522*, 216224.
28. Aramesh, N.; Bagheri, A. R.; Zhang, Z.; Yadollahi, B.; Lee, H. K. *Coord. Chem. Rev.* **2024**, *507*, 215767.
29. Xu, X.; Guo, Y.; Li, B.; Lv, Y.; Wu, Z.; Liang, S.; He, L.; Song, Y.-F. Polyoxometalates Emerging as Multifunctional Powerhouses in the Battle Against Cancer. *Coord. Chem. Rev.* **2025**, *522*, 216210.
30. Yang, G.; Liu, Y.; Wei, Y. Application of Polyoxometalates in Biomass Conversion. *Coord. Chem. Rev.* **2024**, *521*, 216172.
31. Zhong, B.; Liu, J.; Liu, G.; Zhang, Z.; Chen, Y.; Wang, X. *J. Mol. Struct.* **2025**, *1332*, 141679.
32. Li, Z.; Li, H.; Lin, Y.; Shi, W.; Wang, X. Cluster-Cation Pairs Mediated Assembly of Subnanometer Polyoxometalates Superstructures. *J. Am. Chem. Soc.* **2024**, *146*, 28874–28884.
33. Zhang, S.; Shi, W.; Wang, X. *Science* **2022**, *7574*.
34. Tang, W.; Zhang, L.; Qiu, T.; Tan, H.; Wang, Y.; Liu, W.; Li, Y. Efficient Conversion of Biomass to Formic Acid Coupled with Low Energy Consumption Hydrogen Production from Water Electrolysis. *Angew. Chem. Int. Ed.* **2023**, *62*, e202305843.
35. Zheng, K.; Ye, Y.; Shi, Y.; Xu, Y.; Yang, Z.; Ma, P.; Wang, J.; Niu, J. dl-Serine Covalently Ornamented and Ln^{3+}-Incorporated Arsenotungstates with Fast-Responsive Photochromic and Photoinduced Luminescent Switchable Behaviors. *Inorg. Chem.* **2022**, *61*, 15871–15879.
36. Li, S.; Ma, Y.; Zhao, Y.; Liu, R.; Zhao, Y.; Dai, X.; Ma, N.; Streb, C.; Chen, X. Hydrogenation Catalysis by Hydrogen Spillover on Platinum-Functionalized Heterogeneous Boronic Acid-Polyoxometalates. *Angew. Chem. Int. Ed.* **2023**, *62*, e202314999.
37. Song, P.; Wang, T. Application of Polyoxometalates in Chemiresistive Gas Sensors: a Review. *ACS Sens.* **2022**, *7*, 3634–3643.
38. Clemente-Juan, J. M.; Coronado, E.; Gaita-Ariño, A. *Chem. Soc. Rev.* **2012**, *41*, 7464–7478.
39. Zhang, Z.-R.; Sui, H.-Y.; Shi, W.-X.; Ren, J.; Yao, S.; Lu, T.-B.; Zhang, Z.-M. Polyoxometalate-Based Single-Atom Catalyst with Precise Structure and Extremely Exposed Active Site for Efficient H_2 Evolution. *Angew. Chem. Int. Ed.* **2025**, *64*, e202416711.
40. J. Liu, N. Jiang, J.-M. Lin, Z.-B. Mei, L.-Z. Dong, Y. Kuang, J.-J. Liu, S.-J. Yao, S.-L. Li, Y.-Q. Lan, Structural Evolution of Giant Polyoxometalate: from "Keplerate" to "Lantern" Type Mo_{132} for Improved Oxidation Catalysis. **2023**, *62*, e202304728.
41. Meng, W.-Q.; Sedgwick, A. C.; Kwon, N.; Sun, M.; Xiao, K.; He, X.-P.; Anslyn, E. V.; James, T. D.; Yoon, J. Fluorescent Probes for the Detection of Chemical Warfare Agents. *Chem. Soc. Rev.* **2023**, *52*, 601–662.
42. Bobbitt, N. S.; Mendonca, M. L.; Howarth, A. J.; Islamoglu, T.; Hupp, J. T.; Farha, O. K.; Snurr, R. Q. Metal-Organic Frameworks for the Removal of Toxic Industrial Chemicals and Chemical Warfare Agents. *Chem. Soc. Rev.* **2017**, *46*, 3357–3385.
43. An, H.; Hou, Y.; Chang, S.; Zhang, J.; Zhu, Q. Highly Efficient Oxidation of Various Thioethers Catalyzed by Organic ligand-modified Polyoxomolybdates. *Inorg. Chem. Front.* **2020**, *7*, 169–176.
44. Müller, A.; Todea, A. M.; van Slageren, J.; Dressel, M.; Bogge, H.; Schmidtmann, M.; Luban, M.; Engelhardt, L.; Rusu, M. Triangular Geometrical and Magnetic Motifs Uniquely Linked on a Spherical Capsule Surface. *Angew. Chem., Int. Ed.* **2005**, *44*, 3857–3861.
45. Todea, A. M.; Merca, A.; Bögge, H.; van Slageren, J.; Dressel, M.; Engelhardt, L.; Luban, M.; Glaser, T.; Henry, M.; Müller, A. Extending the {(Mo)MO5}12M30 capsule keplerate sequence: a {Cr30} cluster of S=3/2 metal centers with a {Na(H2O)12} encapsulate. *Angew. Chem., Int. Ed.* **2007**, *46*, 6106–6110.
46. Müller, A.; Das, S. K.; Krickemeyer, E.; Kögerler, P.; Bögge, H.; Schmidtmann, M. *Solid State Sci.* **2000**, *2*, 847–854.
47. Müller, A.; Shah, S. Q. N.; Bögge, H.; Schmidtmann, M.; Paul, K.; Hauptfleisch, B.; Leiding, S.; Wittler, K. Thirty Electrons "Trapped" in a Spherical Matrix: A Molybdenum Oxide-based Nanostructured Keplerate Reduced by 36 Electrons. *Angew. Chem., Int. Ed.* **2000**, *39*, 1614–1616.
48. Yin, J.; Huang, C.; Zhou, Y.; Zhang, L.; Li, N.; Sun, R. Selective Oxidation of 2-Chloroethyl Ethyl Sulfide in Aqueous Media Catalyzed by $\{Mo_{72}M_{30}\}$ Nano-polyoxometalate Clusters Differentiating the Catalytic Activity of Nodal Metals. *Ind. Eng. Chem. Res.* **2022**, *61*, 7699–7708.
49. Silversmit, G.; Depla, D.; Poelman, H.; Marin, G. B.; De Gryse, R. Determination of the V2p XPS Binding Energies for Different Vanadium Oxidation States (V5+ to V0+). *J. Electron. Spectrosc.* **2004**, *135*, 167–175.
50. Yang, Y.; Tao, F.; Zhang, L.; Zhou, Y.; Zhong, Y.; Tian, S.; Wang, Y. Preparation of a Porphyrin-Polyoxometalate Hybrid and Its Photocatalytic Degradation Performance for Mustard Gas Simulant 2-chloroethyl Ethyl Sulfide. *Chin. Chem. Lett.* **2022**, *33*, 2625–2629.
51. Bartlett, P. D.; Swain, C. G. Kinetics of Hydrolysis and Displacement Reactions of 'β,β'-Dichlorodiethyl Sulfide (Mustard Gas) and of "β-Chloro-β"-Hydroxydiethyl Sulfide (Mustard Chlorohydrin). *J. Am. Chem. Soc.* **1949**, *71*, 1406–1415.
52. Narske, R. M.; Klabunde, K. J.; Fultz, S. Solvent Effects on the Heterogeneous Adsorption and Reactions of (2-Chloroethyl)ethyl Sulfide on Nanocrystalline Magnesium Oxide. *Langmuir* **2002**, *18*, 4819–4825.

53. Mojarrad, A. G.; Zakavi, S. Simple Low Cost Porphyrinic Photosensitizers for Large Scale Chemoselective Oxidation of Sulfides to Sulfoxides Under Green Conditions: Targeted Protonation of Porphyrins. *Catal. Sci. Technol.* **2018**, *8*, 768–781.
54. Li, H.-L.; Lian, C.; Yang, G.-Y. A Ring-shaped 12-Ti-Substituted Poly(Polyoxometalate): Synthesis, Structure, and Catalytic Properties. *Sci. China: Chem.* **2022**, *65*, 892–897.
55. Chen, Y.; Guo, Z.-W.; Li, X.-X.; Zheng, S.-T.; Yang, G.-Y. *CCS Chem.* **2021**, *3*, 1232–1241.
56. Li, H.-L.; Zhao, S.-H.; Gao, A.; Lian, C.; Cao, X. $\{SeO_2(OH)\}$ Bridging Lanthanide-Containing Antimono-Seleno-Tungstates. *Inorg. Chem.* **2024**, *63*, 9899–9906.
57. Lian, C.; Zhao, S.-H.; Li, H.-L.; Cao, X. A Giant Ce-containing Poly(Tungstobismuthate): Synthesis, Structure and Catalytic Performance for the Decontamination of a Sulfur Mustard Simulant. *Chin. Chem. Lett.* **2024**, *35*, 109343.
58. Tian, H.-R.; Zhang, Z.; Liu, S.-M.; Dang, T.-Y.; Li, X.-H.; Lu, Y.; Liu, S.-X. A Novel Polyoxovanadate-Based Co-Mof: Highly Efficient and Selective Oxidation of a Mustard Gas Simulant by Two-Site Synergetic Catalysis. *J. Mater. Chem. A* **2020**, *8*, 12398–12405.
59. Vorontsov, A. V.; Lion, C.; Savinov, E. N.; Smirniotis, P. G. Pathways of Photocatalytic Gas Phase Destruction of HD Simulant 2-Chloroethyl Ethyl Sulfide. *J. Catal.* **2003**, *220*, 414–423.
60. Tian, H.-R.; Zhang, Z.; Dang, T.-Y.; Liu, S.-M.; Lu, Y.; Liu, S.-X. Hollow Lindqvist-like-Shaped $\{V_6\}$ Cluster-Based Metal–Organic Framework for the Highly Efficient Detoxification of Mustard Gas Simulant. *Inorg. Chem.* **2021**, *60*, 840–845.
61. Li, J.-K.; Huang, X.-Q.; Yang, S.; Ma, H.-W.; Chi, Y.-N.; Hu, C.-W. Four Alkoxohexavanadate-based Pd-Polyoxovanadates as Robust Heterogeneous Catalysts for Oxidation of Benzyl-Alkanes. *Inorg. Chem.* **2015**, *54*, 1454–1461.
62. Zhang, Z.; Ma, X.; Han, X.; Cui, H.; Lu, Y.; Liu, S.; Liu, Y. Straightforward Construction of Hollow Polyoxometalate-Based Metal-Organic Framework Via Pseudo-Homoepitaxial Growth. *Sci. China: Chem.* **2022**, *65*, 1921–1928.
63. Yang, L.; Zhang, Z.; Zhang, C.; Li, S.; Liu, G.; Wang, X. An Excellent Multifunctional Photocatalyst with a Polyoxometalate–Viologen Framework for CEES Oxidation, Cr(Vi) Reduction and Dye Decolorization Under Different Light Regimes. *Inorg. Chem. Front.* **2022**, *9*, 4824–4833.
64. Gong, Y.; Wu, T.; Jiang, P. G.; Lin, J. H.; Yang, Y. X. *Inorg. Chem.* **2013**, *52*, 777–7849.
65. Li, X.; Pi, Y.; Xia, Q.; Li, Z.; Xiao, J. TiO2 Encapsulated in Salicylaldehyde-NH2-MIL-101(Cr) for Enhanced Visible light-driven Photodegradation of MB. *Appl. Catal., B* **2016**, *191*, 192–201.
66. Li, Y.; Gao, Q.; Zhang, L.; Zhou, Y.; Zhong, Y.; Ying, Y.; Zhang, M.; Huang, C.; Wang, Y. H5PV2Mo10O40 Encapsulated in MIL-101(Cr): Facile Synthesis and Characterization of Rationally Designed Composite Materials for Efficient Decontamination of Sulfur Mustard. *Dalton Trans.* **2018**, *47*, 6394–6403.
67. Sharma, A.; Singh, B.; Saxena, A. Polyoxometalate Impregnated Carbon Systems for the *insitu* Degradation of Sulphur Mustard. *Carbon* **2009**, *47*, 1911–1915.
68. Sun, X.; Dong, J.; Li, Z.; Liu, H.; Jing, X.; Chi, Y.; Hu, C. Mono-Transition-Metal-Substituted Polyoxometalate Intercalated Layered Double Hydroxides for the Catalytic Decontamination of Sulfur Mustard Simulant. *Dalton Trans.* **2019**, *48*, 5285–5291.
69. Jung, D.; Su, S.; Syed, Z. H.; Atilgan, A.; Wang, X.; Sha, F.; Lei, Y.; Gianneschi, N. C.; Islamoglu, T.; Farha, O. K. A Catalytically Accessible Polyoxometalate in a Porous Fiber for Degradation of a Mustard Gas Simulant. *ACS Appl. Mater. Interfaces* **2022**, *14*, 16687–16693.
70. Wang, X.-H.; Huang, Y.-B.; Lin, Z.-J.; Cao, R. Phosphotungstic Acid Encapsulated in the Mesocages of Amine-Functionalized Metal–Organic Frameworks for Catalytic Oxidative Desulfurization. *Dalton Trans.* **2014**, *43*, 11950–11958.
71. Zhang, X.; Li, Y.; Li, Y.; Wang, S.; Wang, X. Polyoxometalate Immobilized on Graphene via Click Reaction for Simultaneous Dismutation of H_2O_2 and Oxidation of Sulfur Mustard Simulant. *ACS Appl. Nano Mater.* **2019**, *2*, 6971–6981.
72. Klein, M.; Varvak, A.; Segal, E.; Markovsky, B.; Pulidindi, I. N.; Perkas, N.; Gedanken, A. Sonochemical Synthesis of HSiW/Graphene Catalysts for Enhanced Biomass Hydrolysis. *Green Chem.* **2015**, *17*, 2418–2425.
73. Buru, C. T.; Li, P.; Mehdi, B. L.; Dohnalkova, A.; Platero-Prats, A. E.; Browning, N. D.; Chapman, K. W.; Hupp, J. T.; Farha, O. K. Adsorption of a Catalytically Accessible Polyoxometalate in a Mesoporous Channel-Type Metal–Organic Framework. *Chem. Mater.* **2017**, *29*, 5174–5181.
74. Buru, C. T.; Platero-Prats, A. E.; Chica, D. G.; Kanatzidis, M. G.; Chapman, K. W.; Farha, O. K. Thermally Induced Migration of a Polyoxometalate Within a metal–organic Framework and Its Catalytic Effects. *J. Mater. Chem. A* **2018**, *6*, 7389–7394.
75. Buru, C. T.; Wasson, M. C.; Farha, O. K. $H_5PV_2Mo_{10}O_{40}$ Polyoxometalate Encapsulated in NU-1000 Metal–Organic Framework for Aerobic Oxidation of a Mustard Gas Simulant. *ACS Appl. Nano Mater.* **2020**, *3*, 658–664.
76. Livingston, S. R.; Landry, C. C. Oxidation of a Mustard Gas Analogue Using an Aldehyde/O_2 System Catalyzed by V-Doped Mesoporous Silica. *J. Am. Chem. Soc.* **2008**, *130*, 13214–13215.
77. Chen, Y.; Chang, S.; An, H.; Li, Y.; Zhu, Q.; Luo, H.; Huang, Y. Two Polymorphic Polyoxometalate-Based Metal–Organic Frameworks for the Efficient Synthesis of Functionalized Sulfoxides and Detoxification of Mustard Gas Simulants. *ACS Sustain. Chem. Eng.* **2021**, *9*, 15683–15693.
78. Yu, M.-Y.; Yang, J.; Guo, T.-T.; Ma, J.-F. Efficient Catalytic Oxidative Desulfurization Toward Thioether and Sulfur Mustard Stimulant by Polyoxomolybdate–Resorcin[4]Arene-Based Metal–Organic Materials. *Inorg. Chem.* **2020**, *59*, 4985–4994.
79. Liu, F.; Lu, Q.; Jiao, X.; Chen, D. Fabrication of Nylon-6/POMs Nanofibrous Membranes and the Degradation of Mustard Stimulant Research. *RSC Adv.* **2014**, *4*, 41271–41276.
80. M. T. Naseri, M. Sarabadani, D. Ashrafi, H. Saeidian and M. Babri, Environ. Sci. Pollut. Res. 2013, *20*, 907–916.

Supplementary Material: This article contains supplementary material (https://doi.org/10.1515/revic-2025-0047).